Review

Not peer-reviewed version

Electron-Beam Pumped UVC-Emitters Based on (Al, Ga)N Material System

Valentin Jmerik *, Vladimir Kozlovsky, Xinqiang Wang

Posted Date: 20 June 2023

doi: 10.20944/preprints202306.1422.v1

Keywords: Ultraviolet C emission; electron-beam pumped ultraviolet (UV)C emitters; AlGaN group III-nitrides; low dimensional structures; 2D quantum wells

Review

Electron-Beam Pumped UVC-Emitters Based on (Al,Ga)N Material System

Valentin Jmerik [1,*], Vladimir Kozlovsky [2] and Xinqiang Wang [3]

[1] Ioffe Institute, 26 Politekhnicheskaya, 194021 St. Petersburg, Russia
[2] P. N. Lebedev Physical Institute, Leninsky Ave. 53, Moscow 119991, Russia; kozlovskiyvi@lebedev.ru
[3] State Key Laboratory for Mesoscopic Physics and Frontiers Science Center for Nanooptoelectronics, School of Physics, Peking University, Beijing 100871, wangshi@pku.edu.cn
* Correspondence: jmerik@pls.ioffe.ru; Tel.: +7-9112122795

Abstract: Powerful emitters of the ultraviolet C (UVC) light in the wavelength range of 230-280nm are necessary for the development of effective and safe optical disinfection technologies, high-sensitive optical spectroscopy and non-line-of-sight optical communication. This review considers such UVC-emitters with electron-beam pumping of heterostructures with quantum wells in the (Al,Ga)N material system. The important advantages of these emitters include the absence of the critical problem of p-type doping and the possibility of achieving record (up to several tens of watts for peak values) output optical power values in the UVC range. The review consistently considers about a decade of world experience in the implementation of various UV emitters with various types of thermionic, field-emission, and plasma-cathode electron guns (sources) used to excite various designs of active (light-emitting) regions in heterostructures with quantum wells $Al_xGa_{1-x}N/Al_yGa_{1-y}N$ (x = 0 − 0.5, y = 0.6 − 1) fabricated either by metal-organic chemical vapor deposition or by plasma-activated molecular beam epitaxy. Special attention is paid to the production of heterostructures with multiple quantum wells/two-dimensional(2D) quantum disks GaN/AlN with a monolayer (1ML ~ 0.25nm) thickness, which ensures a high internal quantum efficiency of radiative recombination in the UVC range, low elastic stresses in heterostructures, and a high output UVC-optical powers.

Keywords: Ultraviolet C emission; electron-beam pumped ultraviolet (UV)C emitters; AlGaN group III-nitrides; low dimensional structures; 2D quantum wells

1. Introduction

Optoelectronic devices based on wide-bandgap compounds in the (Al,Ga)N material system are capable of operating in a significant part of the ultraviolet-C (UVC) spectral range with a wavelength (λ) between 210 and 280 nm. Many UVC-photodetector and emitters have been developed over the last two decades of intensive development in this area due to many applications of these devices, reviewed in the next chapter. UVC-Light emitting diodes (UVC-LEDs) have received the most attention from UV-C emitter developers and many excellent books, reviews and roadmaps on the subject have been published in recent years [1–8]. A brief analysis of the literature reveals the limited use of AlGaN-based semiconductor UVC-emitters in the main practical applications. Today, although AlGaN-based UVC-LEDs have achieved a record wall-plug efficiency (WPE) of 20%, which is close to ~30% efficiency for the Hg-lamps emitting at λ = 254 nm, typical values of this parameter for the commercial devices lie in the 1 – 5% range. UVC-LEDs are just beginning to penetrate the UVC-optoelectronic market [9].

The relatively low WPE of UVC LEDs limits their output optical power to no more than ~100 mW at 250 mA in commercial devices. However, according to the forecast published by Kneissl et al. in 2019 [10], this parameter for the UVC-LEDs emitting in the range λ = 256 – 310 nm should be increased to 15 – 20% by 2025, which is quite close to the efficiency of Hg-lamps. This progress, combined with the environmental, dimensional and other advantages of semiconductor devices, will ensure their wider practical application. Meanwhile, the further progress for far-UVC LEDs based on AlGaN heterostructures is not so optimistic, and today the best laboratory device of this type, emitting at 231 nm, demonstrates a maximum cw-optical power of ~3.5 mW at 150 mA [11]. This

 doi:10.20944/preprints202306.1422.v1

decrease in far-UVC-LED power at shorter operating wavelengths is largely due to the increased difficulty of doping *p*-emitters with higher Al-content in such devices. Most researchers consider this problem may be the most difficult challenge in this area [12–16].

Therefore, it is of interest to develop alternative UVC-emitters based on AlGaN heterostructures without *p*-type doped AlGaN layers, in which luminescence is provided by pumping with an external electron-(e-) beam with an energy of up to 20 keV and a current from several milliamps in continuous wave (cw-) mode to a few amperes in a pulsed one. In addition to eliminating the need for doping of such structures, they have other advantages, such as design simplicity, large area emitting surface up to several mm^2 and even cm^2, and the absence of the problem of current leakage.

In this review, first, a brief review of the most promising areas of application of e-beam pumped UVC emitters is carried out. Then, the main types and design features of electron sources (e-guns) used for e-beam pumping of semiconductor light-emitting AlGaN-based heterostructures are considered. Specific information is given about various e-guns that provide the emission of e-beams in an extremely wide current range from tens of nA to several amperes, as well as having different beam diameters from the submillimeter range to two inches. In the main chapter of the review, we successively consider the UVC emitters with various designs of active (light-emitting) regions, which, as a rule, based on heterostructures with multiple quantum wells (MQW) in the (Al,Ga)N system, excited by various e-guns operating in cw- and pulsed mode. The possibilities of fabrication of UVC emitters with various beam size and an output optical power from several milliwatts to several tens of watts are demonstrated. Special attention is paid to a new type of heterostructures based on monolayer (ML)-thick GaN/AlN MQWs.

2. Main applications of UVC-emitters

The main areas of application of existing lamp-based and semiconductor UVC emitters under development are schematically shown in Figure 1. By far, optical (chemical-free) disinfection of air, water and surfaces is the most common and demanded application of UVC radiation. The earliest scientific observations of the bactericidal effects of sunlight radiation began with Downes and Blunt in 1877 [17], and its practical application was accelerated by the simultaneous development of the first mercury (Hg) vapor arc lamps. In 1903, Barnard and Morgan discovered the germicidal effect for the UV light in the spectral range of 226 – 328 nm [18]. These UVC-emitting lamps were first applied in 1906 for drinking water treatment [19]. Since the 1930s, these lamps have been widely introduced into hospital and school practice for optical disinfection of rooms, instruments, etc. A detailed history of the discovery and introduction of UV radiation for optical disinfection can be found in Kowalski's book [20]. The discovery of the structure of DNA molecules in the 1950s scientifically explained the biological activity of UVC light. This effect was associated with various optically induced rearrangements of bonds in DNA molecules included in all pathogenic viruses and bacteria, which excluded their reproduction and activity.

Currently, in the context of the just ended CARS COVID19 pandemic and possible future pandemics of no less dangerous diseases, optical disinfection of air/water and surfaces is being actively developed by many companies and research centers around the world. The state of the art in this area has been described in excellent recent reviews [21–23], which indicate that exposure by UVC radiation at 254 or 222 nm with a dose of about 2–6 mJ cm^{-2} is required to reduce the concentrations of the main pathogenic bacteria by a thousand times. The same UVC radiation can be also used to protect food from bacteriological decay [24,25].

Preprints (www.preprints.org) | NOT PEER-REVIEWED | Posted: 20 June 2023 doi:10.20944/preprints202306.1422.v1

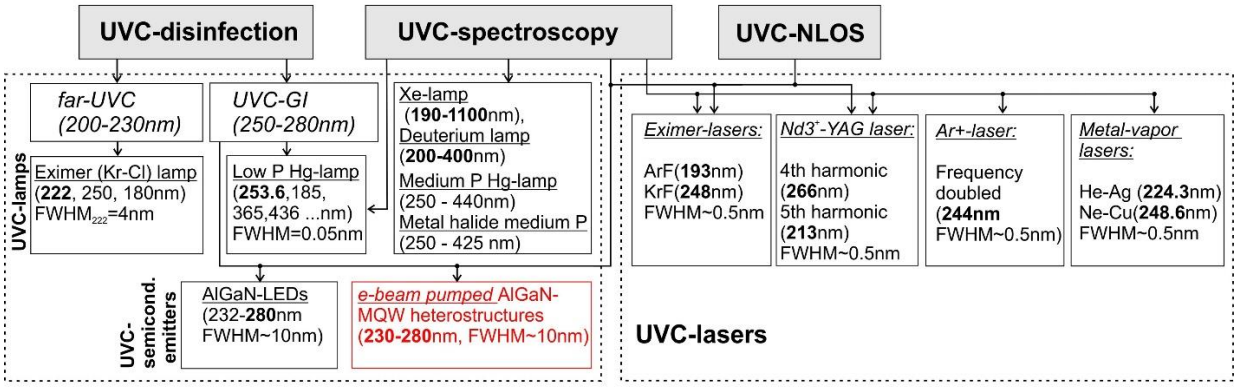

Figure 1. Main areas of application of modern lamp-based UVC-emitters and the developed semiconductor UVC-LEDs and e-beam pumped UVC-emitters.

Due to its high biological activity, UV light has several harmful side effects, namely a carcinogenic effect on human skin and developing eye cataracts [26]. The maximum risk of the former is manifested in the so-called UVB-subrange (λ = 280 – 315nm), and data on photocarcinogenic effect for UVC-GI (germicidal irradiation) range (λ = 250 – 280 nm) are still contradictory and insufficient [27]. It is well-established that UV light with λ = 250 – 315 nm can penetrate down to the basal cell layer, the bottom-most layer of the skin, and damage human DNA. However, these effects disappear almost completely in the so-called far-UVC range (λ = 200 – 230 nm), which has a similar biological effect on pathogenic μm-size microorganisms, but does not penetrate into the human stratum corneum (the outer dead layer of the skin with a thickness of 5 – 20 μm), nor into the cornea of the eye (thickness ~500 μm) [28–30]. According to the 8-hr threshold limit values for corneal and skin UV damages established in 2022 by American Conference of Governmental Industrial Hygienists the minimum safe dose for UV light with (λ = 250 – 300 nm is 10 mJ·cm^{-2}, and for UVC light at 222 nm it is increases to 5·10^2 mJ·cm^{-2} [31]. Thus, the UVC range is divided into these two subranges: high-risk UVC-GI ((λ = 250 – 280 nm) and safe far-UVC ((λ = 200 – 230 nm).

Currently, the main means of optical disinfection are mercury (Hg) lamps emitting mainly in the UVC-GI subrange at λ = 253.7 nm. However, recently these lamps have been intensively replaced by excimer (Kr – Cl) lamps of a new type, emitting mainly in the far-UVC subrange at λ = 222 nm. These new lamps have similar biological activity, but are much safer for human and therefore are considered more promising.

The main advantage of the above lamps is the relatively high WPE up to 35%, providing output UVC optical powers from a few watts to several tens of watts at typical optical power density of ~1 mW cm^{-2} and typical distances from UVC lamps of ~10 – 20 cm [20,30,32 – 35]. Thus, the required lower limit of the UVC-radiation dose of ~10 mJ cm^{-2}, necessary for the full destruction of the main pathogens, can be quickly achieved to ensure the disinfection of running water, air in enclosed spaces (rooms) and various large-area surfaces.

However, UVC lamps have disadvantages and, first, low environmental friendliness due to the presence of mercury in UVC-GI lamps and the need to filter parasitic UVC radiation in the ozone-generating subrange λ < 185 nm, which increases with increasing lamp power of any type. Unfortunately, this problem has not been completely solved in today's lamps, as evidenced by studies of the effect of a side increase in the concentration of ozone and numerous types of nanoparticles in rooms during the operation of high-power UVC-GI lamps [32]. Moreover, for all types of UVC-lamps, in addition to their fragility, large dimensions, high supply voltage, long warm-up times and short service life, it is also necessary to note their principal limitations, such as a limited set of operating wavelengths and impossibility of generating UVC-laser emission.

Another application of UVC irradiation is optical-spectroscopy with the emission of exciting UVC-light and detecting fluorescence signal in the UV-B, near UV and visible ranges. These methods are used to identify various substances, including various hazardous bio- and chemical agents, explosive substances [36–38], drugs [39,40], molecular assemblies, such as peptides/proteins [41], as well as the traces of water and organic molecules in astrobiology research, including the study of Mars [42,43], etc. It is especially important to ensure the development of UVC-emitters operating in

Preprints (www.preprints.org) | NOT PEER-REVIEWED | Posted: 20 June 2023 doi:10.20944/preprints202306.1422.v1

the range of λ = 200 – 250 nm, where strong fluorescence cross sections improve the detection sensitivity. Various types of gas-discharge lamps, including low pressure Hg-, deuterium, halide, etc.(see Figure 1), are used in UV-spectroscopic devices to excite the recorded spectra.

A much higher accuracy is ensured in the case of laser induced fluorescence (LIF) detection using solid-state UVC-lasers, including $Nd3^{+}$-YAG: 4^{th} and 5^{th} harmonics at 266 and 213 nm, respectively [36], metal vapor (Ne – Cu: 248.6 nm, He – Ag: 224.3nm), etc. [38]. Moreover, the use of UVC lasers makes it possible to realize the fusion of Raman-fluorescence detection with fluorescence-free Raman detection to improve the sensitivity of the method [39,41–43]. For the improving the accuracy of the UVC-optical spectroscopy methods, including Light Detection and Ranging (LIDAR), it is necessary to ensure the ability to generate UVC radiation in the entire wavelength range with maximum power. Compact, efficient, durable, high-power UVC lasers would greatly advance LIF detection of environmental and biological threats. At present, several scientific groups are engaged in the development of alternative semiconductor UVC lasers based on AlGaN heterostructures, but this topic is beyond the scope of this review. A detailed analysis of this problem can be found in a recent review by Nikishin *et al*. [44].

In addition, UVC radiation with λ = 200 – 280 nm can be used to implement non-line-of-sight (NLOS) optical communication at distances from several tens of meters to one kilometer or more. This unique ability is due to the strong Mie scattering of UVC radiation by the air atmosphere/aerosol cloud and solar blind nature of this radiation (for space, the long-wavelength border of the solar-blind range is ~260 nm) [45–47]. The choice of the operating UVC wavelength is determined by the trade-off between increased Mie scattering and the shorter communication range with a decrease in this parameter. Various types of UVC-emitters are proposed to be used as transmitters in NLOS systems. They include both UVC-lasers emitting coherent radiation and various sources of spontaneous radiation - mercury lamps or semiconductor UVC LEDs. The most important parameter that determines the communication range and data transfer rate is the output power of the emitters. For example, various solid-state UVC lasers with a frequency multiplier or a nonlinear crystal converter of the initial visible or IR laser emission are used as such transmitters in the NLOS test [46]. An excellent review on the use of various UVC emitters in NLOS systems, including various mercury lamps, solid state lasers, and the latest UVC-LEDs, was recently published by Guo et al. [47].

Research and development of the different solid-state UVC emitters with e-beam pumping are accompanied by their first test applications in the areas described above. Thus, Yoo et al. [48] described the successful deactivation of E.Coli bacteria with 5-log reduction for 60 s using k-sapphire-based UVC-emitter at a peak λ = 230 nm with a light-emitting area of 8.03 cm^2 and a total optical output power of 88.65 mW. This emitter was pumped by carbon nanotube (CNT) e-gun with operating voltage of 10 kV and an anode current of 0.7 mA. DeFreez et al. have developed new e-beam pumped UVC emitters operating in the wavelength range from ~220 nm to detect biological and chemical threats [49]. These test AlGaN-based UVC emitters have demonstrated much higher output optical powers compared to longer wavelength UVC LEDs emitting above 255 nm. Recently, Kang et al. [50] demonstrated a compact light tube for NLOS applications in which a UVC emitter made from a YPO_4:Bi3+ layer provided cw-emission at 246nm with an output optical power of up to 400 mW when excited by a thermionic e-gun with an e-beam energy of 10 keV and an anode current up to 0.8 mA.

3. General Principles of Electron-Pumped UV-Light Emitters

The main problems of creating a wide class of e-beam pumped light-emitting devices are considered in a recent review by Cuesta et al. [51]. First of all, e-beam pumped UVC-emitters (e-beam tubes) are divided according to the radiation output geometry into two types, schematically shown in Figure 2. In the first (*I*) type of such e-beam tubes, shown in Figures 2a,b, UVC radiation is emitted through a surface that is bombarded by electrons from an e-gun cathode located above this surface [52,53]. Such a design can be implemented using e-beam emitting cathodes in the form of either a grid or segmented cathodes that provide oblique beam propagation. The main advantage of such e-beam tubes is the possibility of organizing effective heat removal through the substrate and the absence of requirements for its transparency.

Preprints (www.preprints.org) | NOT PEER-REVIEWED | Posted: 20 June 2023 doi:10.20944/preprints202306.1422.v1

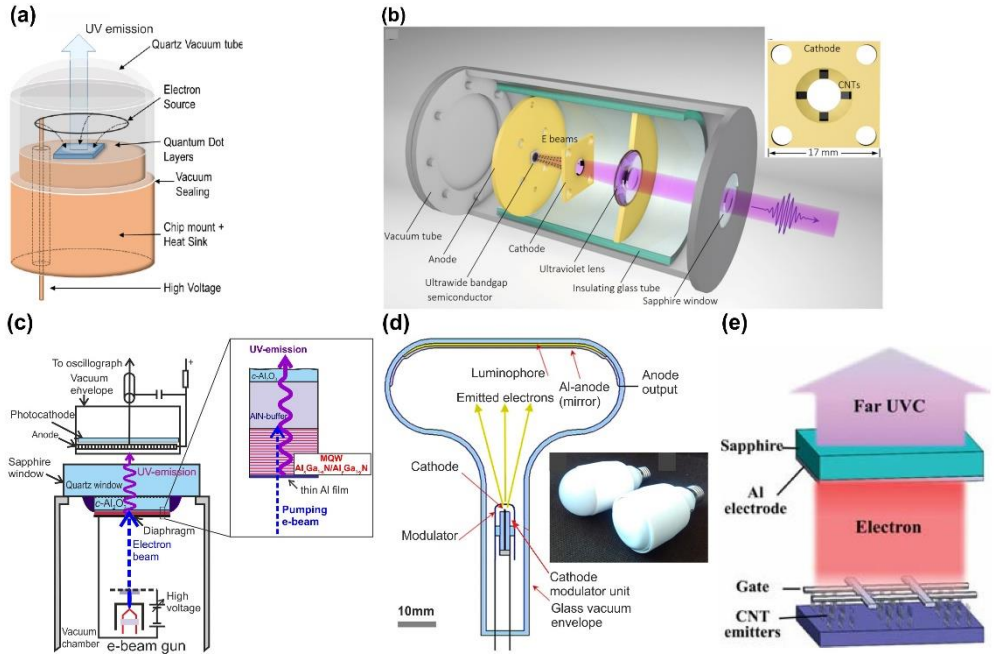

Figure 2. E-beam lamps of type *I*: with a grid cathode [52] (a) and a four-segmented CNT cathode [53] (b). The inset in (b) shows a photo of the latter cathode. E-beam lamps of type *II*: (c) scheme for measuring the characteristics of an e-beam pumped UVC-emitter using a thermionic e-gun and a photocathode for the optical measurements [54]. The inset shows an excitation scheme of (Al,Ga)N-based MQW heterostructure. E-beam lamps with a built-in e-gun and a voltage converter for the E27 standard [55] (d). Schematic of excitation of a UVC-emitter using a field emission e-gun based on large-area CNT cathode [56] (e).

However, in practice, the light emitters shown in Figure 2c-e with a type *II* e-beam pumping scheme are most widely used [54–56]. In these emitters, the e-beam also bombards the surface with the active (light emitting) region, but the output radiation is emitted through the opposite rear substrate surface. Figure 2c shows the scheme of excitation of a GaN/AlN MQW heterostructure in a vacuum chamber using an e-gun that emits an e-beam with controlled energy, current and various operating modes – continuous wave (cw-) or pulsed [54]. The heterostructure is placed on a quartz vacuum window, through which UVC radiation exits to measure its characteristics using a photocathode and a spectrograph. Several types of e-guns can be used in one installation (a detailed description of the various types of e-guns will be given in the next chapter). During measurements, it is important to ensure the stability of the properties of the surface bombarded by an e-beam with energy of up to 20 – 30 keV. In addition, it is necessary to exclude the charging of the heterostructure dielectric surface under the action of this e-beam. Both tasks are quite successfully solved by sputtering a thin (0.2 – 0.7 μm) metal (Al) film onto the bombarded surface.

A compact design of e-beam pumped light emitter of type II is shown in Figure 2b, where all parts are included in the standard lamp bulb R63 with bulb comprising a built-in AC – DC high-voltage converter (up to 20 kV) of the electric line voltage (50 Hz, 230 V) [55]. Figure 2d shows another type II UVC emitter excited by e-gun with a large area cathode based on carbon nanotubes (CNTs) [56].

The thickness and position of the active region in the AlGaN-based e-beam pumped UVC-emitters are determined by the energy of the electrons. Figure 3 shows the spatial distributions of the deposited e-energy in AlGaN layers with various initial e-beam energies, which were calculated using the standard CASINO program [57].

Preprints (www.preprints.org) | NOT PEER-REVIEWED | Posted: 20 June 2023 doi:10.20944/preprints202306.1422.v1

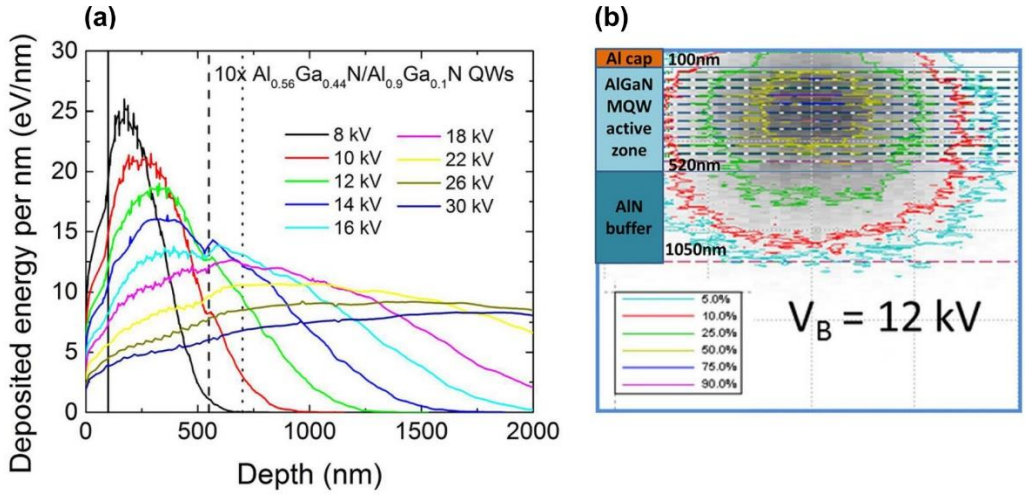

Figure 3. (a) Results of Monte Carlo calculations of absorption distribution profiles for e-beam energies with energies from 8 to 30 keV. The vertical dotted lines show the boundaries of the 10×{$Al_{0.56}Ga_{0.44}N/Al_{0.9}Ga_{0.1}N$} light-emitting MQW region with a length of 150 nm in the AlN layer of the UVC emitter. (b) Two-dimensional absorption distribution of a point e-beam with an energy of 12 keV. The area of maximum excitation (50%) is marked with a yellow contour in the MQW structure [57].

4. The main types of electron guns used to excite UVC radiation

A reliable electron source (e-gun) for excitation of a specimen with an optically active (Al,Ga)N-based heterostructure is one of the most important parts of any e-beam pumped UVC-emitter. Figure 4 classifieds the main types of such e-guns with different basic principle of electron emission, operating parameters, and output characteristics. Among the latter, the most important characteristic is the e-beam current, which primarily determines the output optical power of the UV emitter. This chapter describes successively the e-guns that have already found use in UVC emitters and can do so. The specific parameters and characteristics of these e-guns are summarized in Table 1 at the end of this chapter.

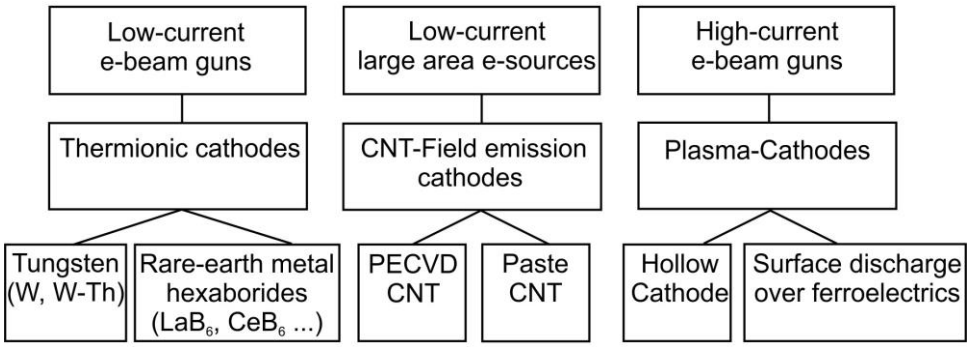

Figure 4. Main types of electron sources for pumping (Al,Ga)N-based UVC-emitters.

4.1. Thermionic e-beam emission guns

The first type of e-beam sources is called thermionic, since electron emission in it is provided by heating the incandescent cathode. In practice, the several types of thermionic e-guns differ primarily in the design of the cathode assembly. Figure 5 shows typical designs of the e-guns with thermionic (incandescent) cathodes, usually made of a v-shaped tungsten filament with a work function (W) of 4.5 eV (thoriated tungsten has a work function of 2.7 − 4.5 eV) or one of the crystals of rare-earth metal hexaborides (LaB_6, CeB_6) with a mich lower work function about 2.4–2.7 eV for LaB_6 [58–60]. At sufficiently high temperatures of the cathode material (1400 – 2400°C) a certain percentage of the electrons acquires sufficient energy to exceed the work function and is emitted in accordance with the Richardson's law which relates the current density from the gun (J) to the operating temperature (T) in Kelvin

Preprints (www.preprints.org) | NOT PEER-REVIEWED | Posted: 20 June 2023 doi:10.20944/preprints202306.1422.v1

$$J = A \cdot T^2 e^{-\frac{W}{kT}}, \quad (1)$$

Here k is Boltzamn constant ($8.6 \cdot 10^{-5}$ eV·K^{-1}) and A is Richardson's constant (A·m^{-2}K^{-2}), which is only constant for a given cathode material. The electrons leaving the filament are accelerated by a potential difference, in the typical range from a few hundred Volts to 30 kV, between the filament and an anode. This voltage determines the energy of electrons in the beam (E_e) bombarding the surface of the light-emitting structure in UV-emitter. The filament is surrounded by a grid cap, the Wehnelt cylinder, biased at a negative potential (0 – 2.5 kV). The electric field generated by the filament, the Wehnelt cylinder, and the anode causes the emitted electrons to converge to the crossover point with a diameter of 10 – 50 μm and a certain divergence angle below the cylinder. An electromagnetic coil is used to focus the e-beam into a spot whose diameter on the light-emitting surface varies from <10 μm up to ~1 mm.

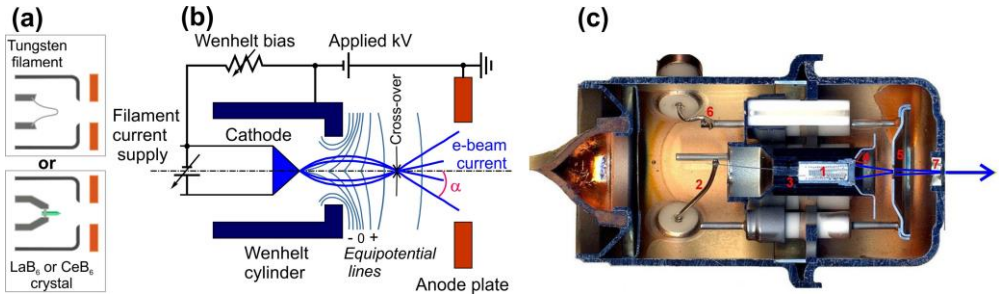

Figure 5. (a) Schemes of cathode assemblies of various types: tungsten (upper) or rare-earth metal hexaborides (lower). (b) General scheme of a thermionic e-beam gun. (c) Cross-sectional photograph of an thermionic e-beam gun with an incandescent cathode: 1 – heated element, 2,3 – wires to the heater, 4 – Wehnelt cylinder, 5 – anode, 6 – high voltage contact, 7 – e-beam output.

Pure or thoriated tungsten cathodes provide stable e-emission under normal vacuum conditions (~10^{-5} mbar) with extended filament lifetime at high temperature. The typical e-beam current (I_e) varies from several tens of nanoamperes to few milliamps [60]. Higher e-beam currents up to several tens of mA can be obtained using a thermionic cathode made of lanthanum hexaboride (LaB_6) [61–62]. Although heating the thermionic source gives a higher e-beam current, higher temperatures shorten the source life through evaporation and/or oxidation. Therefore, a compromise operating temperature is chosen. These e-guns are widely used in analytical study of CL spectra, electron microscopy, television, medicine, etc. The main disadvantage of thermionic e-guns, except for relatively low currents, is the limited size of the output beams (~1 mm), which leads to the need to spatial scan of the e-beam by alternating electric fields over the surface to expand the radiation pattern and to improve the dissipation of thermal power in the light emitting structures.

4.2. Field emission (Cold) electron sources

Field emission (cold) electron sources operate in a fundamentaly different way to thermionic e-beam gun [58]. The based principle of these sources is that the strength of an electric field E is significantly enhanced at sharp points because, if there is a voltage V appled to spherical point of radius r, then

$$E = \frac{V}{r} \quad (2)$$

Currently, many technologies allow one to fabricate fine needles "tips". One of the easiest materials to produce array of nano-sized tips with a radius of < 100 nm is carbon. If we apply a 1-kV potential to this tip then E is ~10^{10} Vm^{-1} and this lowers the work-function barrier sufficiently for electrons to tunnel out of the carbon. The main parameters and characterics of carbon-based e-emitters are summarized in Table 1.

One of the first UVC-emitter with a carbon (graphene)-based field e-emitter was developed by the Matsumoto group in 2012 [63]. Figure 6a shows a nanotip fabricated by etching carbon nanorods in hydrogen plasma, which led to the formation of array of nanotips with a radius of top of 5 nm, having crystallographic structure corresponding to graphene. A stable behavior of such cathode

Preprints (www.preprints.org) | NOT PEER-REVIEWED | Posted: 20 June 2023 doi:10.20944/preprints202306.1422.v1

under a current of 0.5 mA and e-beam energy of 15 keV for 5000 hours was demonstrated, as shown in Figure 6b. This e-emitter was evacuated to a base pressure of 10^{-7} Pa, and then, the glass tube was chipped off.

The compact size of such a e-gun makes it possible to combine it in one housing (30 mm in diameter and 60 mm long) with a UVC-emitting heterostructure grown on a sapphire substrate, which are shown in Figure 5c. It should be noted that the power supply of such an e-beam tube is also compact and has dimensions of 100×150×35 mm and a weight of 650 grams. Because of its low current consumption during operation, the device can be handheld and driven by AA dry batteries.

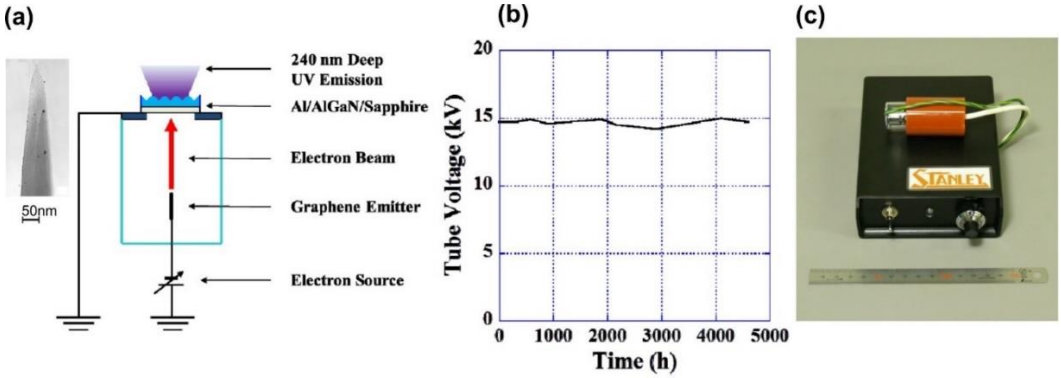

Figure 6. (a) Design of an e-gun with a field (graphene) cathode, the TEM image of which is shown in the inset. **(b)** Change in cathode voltage with time at a current of 500 μA. (c) Photograph of a UVC emitter with a compact cylindrical e-beam gun and a portable power supply that provides adjustment of the e-beam energy in the range of 0 – 10 keV and its current of 0 – 500 μA [63].

Several groups are currently intensively developing various types of large area e-sources using field emission from carbon nanotubes (CNTs) distributed over the surface of various substrates (Si, stainless-steel) up to two inches in diameter [48,53,56,64–68]. As a rule, these emitters use a triode electrode scheme, in which a lower voltage (1 – 2 kV) is applied to the first metal mesh electode (gate) located close (less than 1mm) to the surface of the e-emitting cathode, as shown in Figure 7. This voltage determines the extraction of electrons with characteristic currents of 1 – 5 mA. A higher voltage (up to 7 kV) applied to the second far electrode (anode) determines the energy of the electrons bombarding the light emitting structure located on this electrode. Most of the electrons emitted from the CNT cathode reach the anode with at a typical distance between these electrodes of about 20 mm.

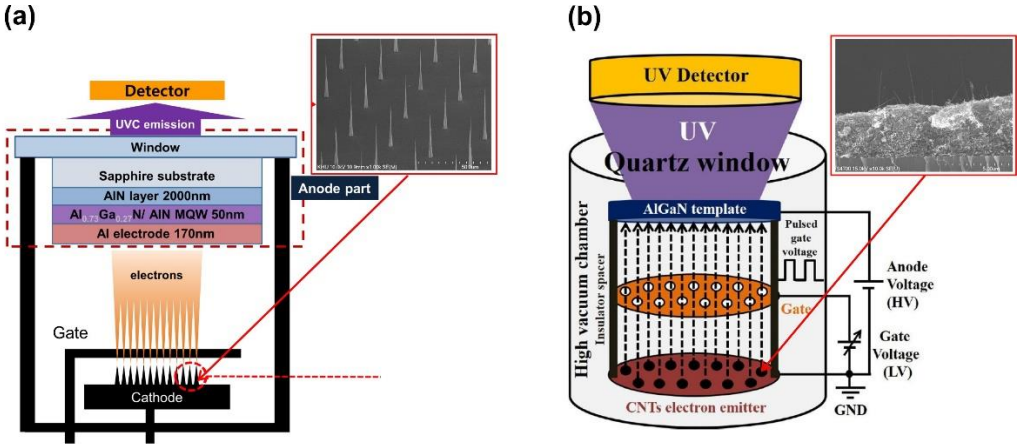

Figure 7. Triode schemes of e-beam guns with CNT e-emitters (cathodes) of various types, formed: (a) by photolithography as regularly arranged nano-tips [67]; (b) multistep process of mixing CNT powder and organic solvents followed by annealing, adhesive type and soft roller treatment, which led to the random formation of vertical CNTs [66]. The insets in each figure show SEM images of the corresponding CNT e-emitters.

Preprints (www.preprints.org) | NOT PEER-REVIEWED | Posted: 20 June 2023 doi:10.20944/preprints202306.1422.v1

There are several approaches to the fabrication of CNT arrays on the substrates. In the first of these, illustrated in the inset to Figure 7a, the regularly arranged positions of individual nanotip CNTs are controlled usually using conventional photolithography [48,56,64,65,67]. The nanotips are formed using plasma-enhanced chemical vapor deposition (CVD) in location with selectively fabricated Ni catalyst on Si substrates. CNT emitters fabricated in this way have a typical height of 40 μm, apex diameter of 50 – 100 nm and a bottom contact diameter of a few microns. The individual CNTs are arranged periodically at 30 μm intervals in large islands (dots) consisting of 49 CNT emitters. The islands are patterned at 0.5 mm intervals to decrease cathode current leakage through the gate electrode. CNT e-emitters of this type have a typical e-emitting area of 200 – 300 mm^2. Figure 8a shows typical current-voltage characteristics for all currents in the triode CNT e-emitter, measured in a continious wave (cw-) mode, and its photo (Figure 8b) with output fluorescent screen emitting under UVC-excitation [48].

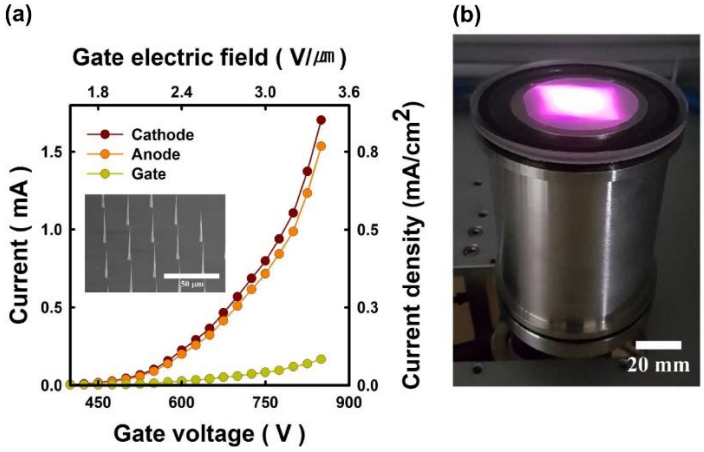

Figure 8. (a) Current-Voltage characteristics of anode, cathode and gate e-beam currents measured in a nanotip CNT e-emitter. (b) photo of UVC emitter with this e-beam CNT emitter [48].

Alternatively, CNT e-beam emitters may be fabricated using a complex multi-step process in which multi-walled CNT powder are first prepared by the thermal CVD [53,66,68]. The CNT have an outer diameter of 7 nm, approxiamtely 5 walls, and a length of more than 10 μm. They are characterized by a high crystallographic quality. Then the CNT paste is syntesized by mixing the CNT powder with various organic and non-organic solvents and fillers. The CNT paste is distributed over the stainless substate using a simple screen-printing process to form desired arrays of CNT dots with a diameter of about 300 μm. The CNTs dots are consequently thermaly treated in air and vacuum ambients to remove all organic ingredients for stabilization of the e-emissive characteristics. Finally, an adhesive tape and soft roller are employed for vertical alignment of nanotubes, providing their physical activation. This type of CNT e-emitters ensures a maximum output e-current of up to 5.5 mA in a cw-mode and a largest emitting surface diameter of up to 2 inches, as shown in Figure 9a [68].

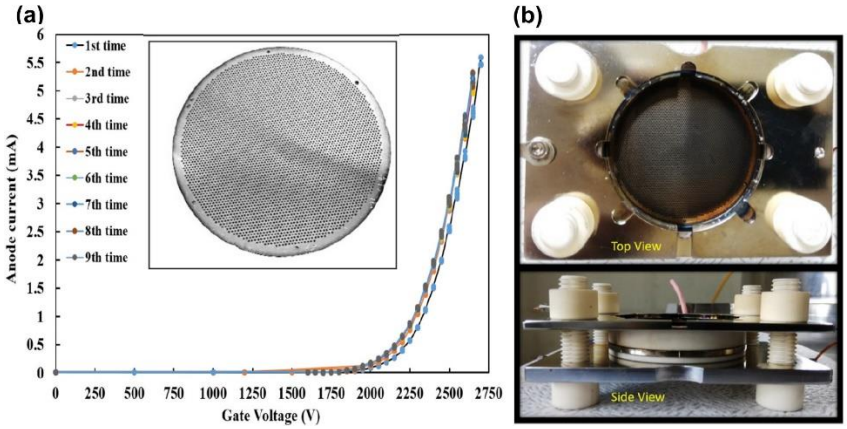

Preprints (www.preprints.org) | NOT PEER-REVIEWED | Posted: 20 June 2023 doi:10.20944/preprints202306.1422.v1

Figure 9. (a) Current-Gate Voltage characteristics of 2-inch CNT e-emitters. The inset shows an image of the on a stainless steel substrate for CNT deposition. (b) Plan- and side-view photos of the setup for CL measurements from the assembly of the UVC-emitter with a CNT e-emitter, the triode scheme of which is shown in Figure 7b [68].

Comparing two methods of CNT fabrication employing either direct selective growth using plasma-enhanced CVD or screen printing of CNT paste, one can highlight the positive and negative sides of each method. The first method makes it possible to directly obtain vertically oriented CNTs with a precisely defined arrangement of individual nanotips and their uniform distribution over the area of the substrate. The main advantage of the second method is its high-cost efficiency and high productivity of the process on large-diameter substrates. However, it should be considered that CNTs fabricated in this way are much worse vertically aligned than nanotips obtained by the plasma-enhanced CVD, and to improve their alignment, it is necessary to perform additional technological operations of annealing, aging, etc.

In summary, it should be noted that all CNT e-emitters have the smallest dimensions at largest e-emitting area compared to other types of e-guns(sources), zero warm-up time and operation at room temperature and relatively low operating voltages and currents. The CNT e-emitter can operate in a high vacuum of 10^{-7} Torr. These devices do not have high-temperature parts and do not consume a high heating current, as in thermionic e-emitters. Unfortunately, very little is known about the temporal stability of CNT electron sources, and this issue needs to be investigated. The main disadvantage of all CNT e-emitters is the relatively low output beam currents, which does not exceed a few milliamps. However, large e-beam areas (up to 2-inch and more) and their operation in a cw-mode indicate the possibility of a wide application of such emitters.

4.3. Electron guns with plasma cahodes

Maximum e-beam currents − up to several amperes and above − can be achieved using the so-called e-guns with "plasma cathodes", which are based on the extracting an e-beam from a plasma generated either in a hollow cathode discharge [69–72] or in a surface discharge near the ferroelectric surface [73–81] without thermionic cathodes and other heated parts.

4.3.1 e-source with a hollow cathode

The e-guns based on a high-voltage discharge with a hollow cathode can be operated in both cw- and pulsed discharge modes. Figure 10a shows the electrode configuration of the former consisting of a hollow stainless-steel cathode 50 mm in diameter and 100 mm long with a centric hole 16 mm in diameter, a plane anode, and a meshed (0.5×0.5 mm²) tantalum electron extractor [69,70]. To produce an axial magnetic field up to 0.1 T solenoid coils were used. The working air pressure varied in the forepump range from 0.01 to 0.1 Torr at a residual pressure of 1 mTorr in a vacuum vessel with an e-gun. Current-Voltage characteristics of this discharge and extracted e-beam demonstrate the complex dependences on the main parameters of this e-gun. Figure 10b shows that a larger cw-e-beam current up to 400 mA can be reached at a higher discharge current, providing higher plasma density. Importantly, that this linear dependence was observed at the optimum values of working air pressure of 10 mTorr and a magnetic field of 17 mT.

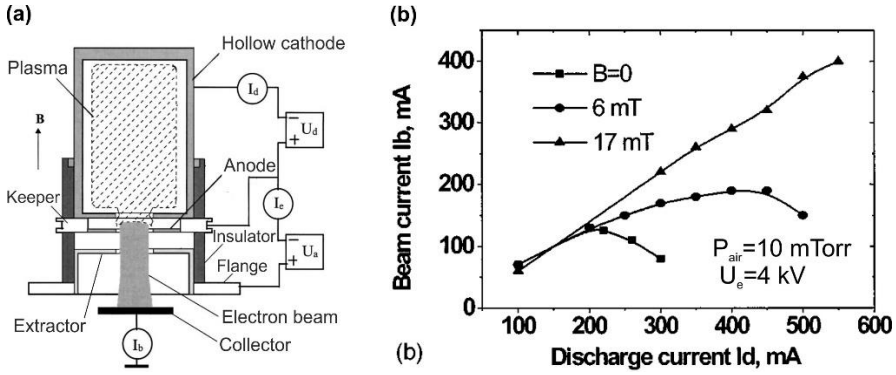

Preprints (www.preprints.org) | NOT PEER-REVIEWED | Posted: 20 June 2023 doi:10.20944/preprints202306.1422.v1

Figure 10. Scheme of an e-gun with a hollow plasma cathode (a) and the dependence of the current of the e-beam on the discharge cw-current at a different axial magnetic field in a hollow plasma cathode (b) [70].

Much higher peak e-currents can be achieved in the so-called pseudo-spark pulsed discharge in the plasma cathode e-gun shown in Figure 11a [71], which is very similar in appearance to the cw-operated e-gun described above. The discharge occurred at an Ar operating pressure of about 80 Pa in a cylindrical discharge chamber with a height and a diameter of about 59 mm. Measurements of the output pulsed e-current revealed its almost linear dependence on the discharge voltage, and its maximum peak value up to 150 A was observed at a discharge voltage of 20 kV and zero distance from the anode. This value decreased to approximately 100 A at 100 mm from the anode. Importantly, this e-gun can operate without the application of an external guiding magnetic field.

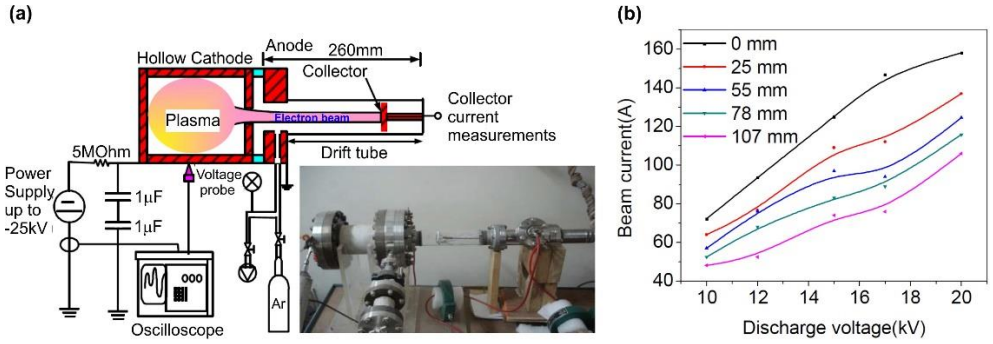

Figure 11. Scheme and photo of a pulsed pseudospark e-gun with a hollow plasma cathode (a) and the dependence of the peak current of the e-beam on voltage at different location of the drift space (b) [71].

The main advantage of all e-guns with a plasma cathode is their ability to operate at a fore pump gas (air or argon) pressure range of (~10^{-2} – 10^{-1} Torr). These e-guns, without any high-temperature parts, have a long service life and can generate stable e-beams with a maximum cw- and peak e-currents of 400 mA and 150 A, respectively [70,72]. These unique properties of the e-guns with plasma cathode ensure their promising applications in various fields of plasma technologies, electron-beam melting, laser pumping etc. However, the need for high-speed vacuum pumping limits the use of electron guns of this type only in powerful stationary installations. We have not been able to find papers describing the use of such e-guns with hollow plasma cathode for pumping UVC emitters, but, in our opinion, this may be a very promising application of these e-guns.

4.3.2. e-guns with ferroelectric cathode

The spontaneous polarization of different ferroelectric materials – $LiNbO_3$ [73], lead-germanate [74], lead-zirconium-titanate (PZT or LZT) [75,76], lead-lanthanium- zirconium-titanate (PLZT) [77,78], barium strontium titanate [79] *etc*. – observed below their Curie temperatures results in screening charges at their surface to keep the charge neutralization at the material boundaries. The spontaneous polarization in these materials can be as high as 20 μC·cm^{-2}, resulting in the accumulation of a screening charge density of 10^{14} elementary charges·cm^{-2}. Altering the spontaneous polarization rapidly results in emission of the unbound surface screening charges. This emission mechanism is unique and can be realized using a patterned metal electrode (strip, grid, or ring) deposited on the polar ferroelectric surface, while a solid metal contact is deposited on the rear side, as shown in Figure 12. This type of electrodes induces not only the normal component, but also a tangential one of the applied electric field, which may cause a dramatic effect of accelerating the emitting electrons along the ferroelectric surface, followed by flashover-plasma generation.

Preprints (www.preprints.org) | NOT PEER-REVIEWED | Posted: 20 June 2023 doi:10.20944/preprints202306.1422.v1

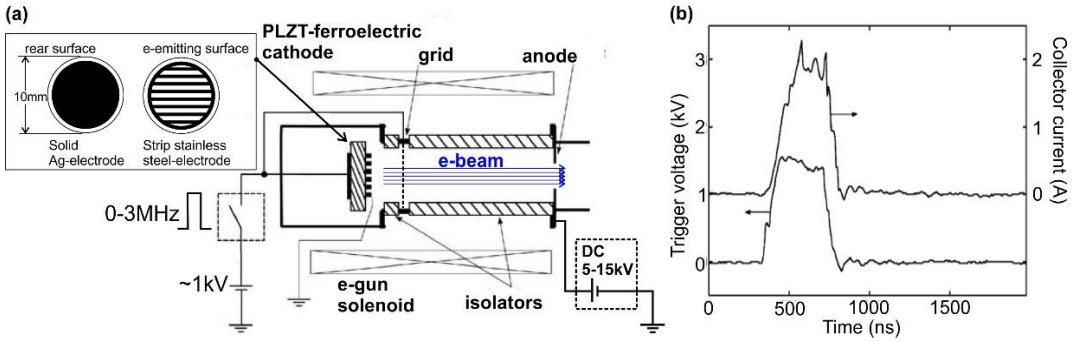

Figure 12. (a) Scheme of an e-source with a plasma cathode based on a surface discharge over a ferroelectric. (b) Time dependence of the output e-current from such a source [77].

The emitted electrons are then accelerated by an e-gun held at a direct current (dc) potential by an external circuit. There are two circuits needed for the experiment: one to provide the gate pulse to induce the electron emission and the second to provide the electron gun voltage (between the cathode and ground anode) to accelerate the emitted e-beam up to typical energy of 5 – 15 keV. These cathodes make it possible to achieve e-beam currents from hundreds of milliamperes to several amperes (with a record electron emission density of up to 1 kA·cm^{-2}) for e-beams with an energy of ~10 keV. These e-guns operate in modest vacuum conditions 10^{-4} – 10^{-5} Torr and, in principle, can be realized as compact e-beam tubes without continuous vacuum pumping. The lack of reproducibility of the shape of the e-beam current pulse makes it difficult to study such a discharge, and the low service life of the ferroelectric surface is a disadvantage for its practical application.

A theory of the e-emission process from ferroelectrics surfaces has been developed by Schachter et al. [80] and detailed reviews of the physical principles of the ferroelectric e-guns have been given by Riege [81], Rosenman et al. [82], and Mesyats [83] *etc*.

Preprints (www.preprints.org) | NOT PEER-REVIEWED | Posted: 20 June 2023 doi:10.20944/preprints202306.1422.v1

Table 1. Main characteristics of the principal e-beam sources.

	Units	Thermionic cathodes		Carbon-based cold field emitters			Plasma cathodes	
		W	LaB_6	Graphene nanoneedle	CNT-CVD	CNT-Paste	Hollow cathode	Ferroelectric cathode
Work function, (W)	eV	4.5	2.4-2.7	-	5	-	-	-
Richardson's constant, (A)	$A{\cdot}m^{-2}K^{-2}$	$6{\cdot}10^{9}$	$4{\cdot}10^{9}$	-	-	-	-	-
Operating temperature, (T)	K	2700	1700	300	300	300	300	300
Crossover (beam) size	mm	>0.1	0.01	-	-	-		
Brightness	$A{\cdot}m^{-2}sr^{-1}$	10^{10}	$5{\cdot}10^{11}$	10^{13}				
Emission current stability	$\%{\cdot}hr^{-1}$	<1	<1	good				poor
Vacuum	Pa	10^{-2}	10^{-4}	10^{-4}	10^{-5}	10^{-5}	10^{-1}	10^{-2}-10^{-3}
Lifetime	hr	100	1000	>5000				>10^{7}pulses
Gate voltage	kV	-	-	-	~1.5	2.7		0.8 – 1.5
Anode voltage	kV	10 – 20	10 – 20	3 – 10	~5	7		5 – 15
Maximum anode (e-beam) current	A	1 – 5	60	0.5	1.5	~5.5	cw:0.4 peak: 120	peak: 2
Technology				H_2-plasma etching	PECVD	MOCVD+ screen-printing		
Radius of tip	nm	-	-	5	60	5 – 7	-	-
e-emission area	mm^2	~1	~1	-	~300	Up to 2-inch	>250	~20
Operation mode		Cw-& Pulsed	Pulse	Cw-& Pulsed	Cw-& Pulsed	Cw-& Pulsed	Cw-& Pulsed	Pulsed

Preprints (www.preprints.org) | NOT PEER-REVIEWED | Posted: 20 June 2023 doi:10.20944/preprints202306.1422.v1

5. Main results on UV-C emitters with Electron Beam Pumping

5.1. Low power UVC emitters (<20mW)

5.1.1. Pumping by a focused e-beams from guns with thermoionic cathodes

Electron-beam pumped UVC emitters were first demonstrated in 2009 by Watanabe et al. [84], who studied the CL spectra of hexagonal boron nitride (h-BN) powder. Figure 13 shows that these spectra exhibit broad peaks at 225 nm at room-temperature (RT) with an almost linear increase in intensity to 0.2 mW as the e-beam energy increases to 7 keV. This UVC-emitter, pumped by an e-beam with an energy of 7 keV and a current of 50 μA, had a WPE of only 0.6%. Moreover, powder materials have high absorption values and a low probability of radiative recombination upon e-beam excitation. Therefore, in subsequent studies, the main efforts of researchers were focused on the development of UVC-emitters based on epitaxial layers and heterostructures in the (Al,Ga)N material system.

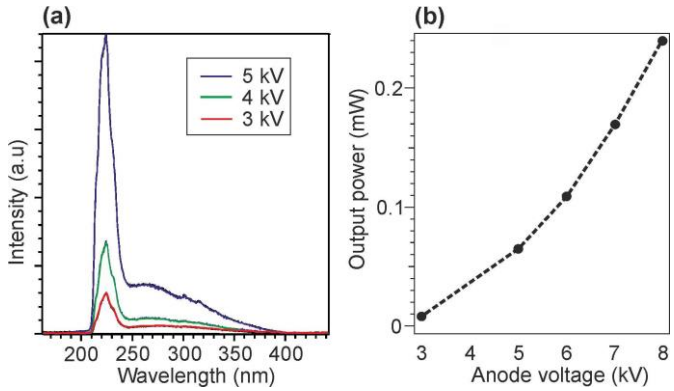

Figure 13. (a) CL-RT spectra emitted by pyro-BN powder pumped with an e-beam with different electron energies, which demonstrate the main peak at 225 nm, the broadening of which is explained by the superposition of exciton levels in the range from 215 to 227 nm. The low-intensity long-wavelength tail in the spectra from 250 to 400 nm is explained by emission from impurities and defects in pyro-BN material. (b) Dependence of the CL output power on the accelerating voltage in the e-gun from 3 to 8 kV, which changes the power value up to ~0.2 mW [84].

In 2010, the Kawakami group published the first results on e-beam pumped UVC emission from an $Al_{0.69}Ga_{0.31}N$/AlN MQW structure grown on a *c*-sapphire substrate with an AlN buffer [85]. Using an e-beam generated by a thermionic e-gun with a maximum e-energy of 10 keV and a e-current of 50 μA, these authors demonstrated UVC radiation at 238 nm and an output optical power of 100 mW, as shown in Figure 14. However, some doubts should be noted about the correctness of the measurement of optical power in this work, since it claims an anomalously high energy conversion efficiency of 40%, while other authors in numerous later works report significantly lower values (< 1% for this type of e-gun). This discrepancy can apparently be due to an erroneous measurement in [85] due to the placement of the UVC radiation detector in a vacuum volume, where its readings could be affected by secondary electrons and X-ray irradiation [57].

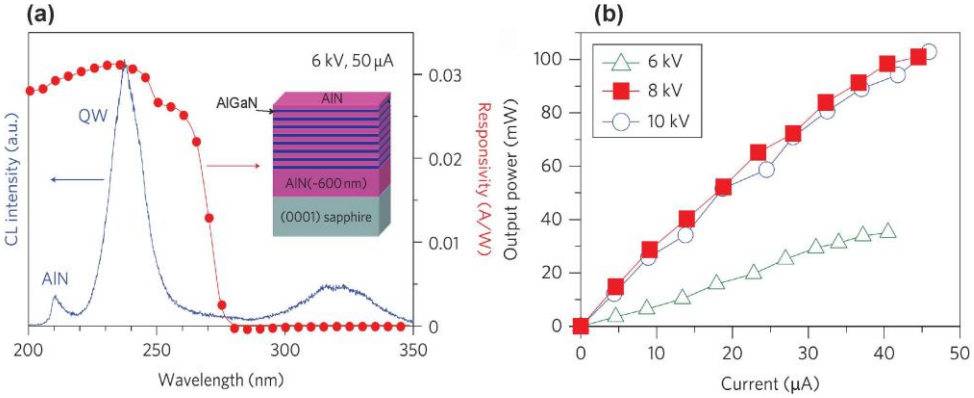

Preprints (www.preprints.org) | NOT PEER-REVIEWED | Posted: 20 June 2023 doi:10.20944/preprints202306.1422.v1

Figure 14. (a) CL-RT spectrum observed when the $Al_{0.69}Ga_{0.31}N$/AlN MQW structure was excited by an e-beam with an energy of 6 keV and a current of 50 μA. The figure also shows the spectral sensitivity of the UV photodiode used in the measurements. (b) Dependences of the output power of the e-beam pumped UVC-emitter on the e-beam current with different energies [85].

This conclusion is confirmed by Shimahara et al. [86], who in 2011 demonstrated compact UVC emitters based on Si-doped ($4 \cdot 10^{17} cm^{-3}$) AlGaN layers 800 nm thick, grown by MOCVD on AlN/*c*-Al_2O_3 templates. The best layer emitted for 2000 hours UVC radiation at 247 nm with an output power of 2.2 mW at an e-beam pumping current of 100 μA and an accelerating voltage of 10kV, which corresponded to an energy conversion efficiency of 0.24%. Later, in 2013, this group demonstrated a UVC-emitter based on an $Al_{0.60}Ga_{0.40}N/Al_{0.75}Ga_{0.25}N$ MQW heterostructure with a total thickness of 600 nm, which emitted at 256 nm with an output power of up to 15 mW and an WPE of 0.75% [87].

All initial results on development UVC emitters, described above, were obtained using thermionic e-guns and low efficiency of these emitters (<1 %) was explained by the consumption of electric power at the thermal filament. A greater efficiency (up to 4%) was found by Matsumoto et al. [63] in 2012 for a UVC-emitter pumped by a field emission (cold) cathode with the graphene nanotips, described in section 4.2. Figure 15 shows CL spectra of the $10\times\{Al_{0.7}Ga_{0.3}N(3nm)/AlN(3nm)\}$ MQW heterostructure, peaked at 240 nm with a maximum power of 20 mW supplied by this cold cathode e-gun with an e-beam energy and a current of 7.5 keV and 80 μA, respectively. All spectra measured at various e-energies exhibit not only the main peaks near 240 nm, but also broad long-wavelength tails around 350 nm with intensities at the maximum about an order of magnitude lower than the intensities of the main peaks. Moreover, as the e-energy increases, a weak peak near 210 nm appears in the CL spectra, which is attributed to the emission of the AlN buffer layer. Figure 15c shows the calculated and experimental dependences of the emission intensity of 240 nm line on the e-energy. The theoretical curve was plotted using Monte-Carlo method to calculate the penetration depths of the e-beams at various electron energies. Unexpectedly, the maximum intensity is reached at energies of 8 – 10 keV, when the main part of the e-beam energy should be adsorbed in the thick AlN layer, and not in the relatively thin 90-nm-thick surface region with the MQWs. The authors explained this by the diffusion of excitons formed in the AlN layer at a distance of about 1 μm to the AlGaN/AlN MQW, but, in our opinion, this explanation needs additional studies.

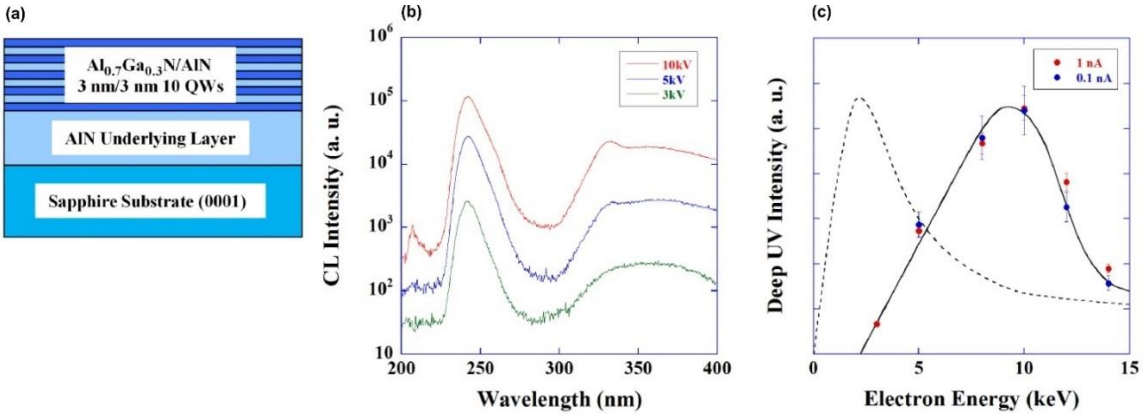

Figure 15. (a) Schematic of the $10\times\{Al_{0.7}Ga_{0.3}N(3nm)/AlN(3nm)\}$ MQW heterostructure; (b) CL-RT spectra of this MQW heterostructure at different electron energies, (c) Theoretical (dashed line) and experimental dependences (solid line) of the CL intensity on the electron energy [63].

The results of this work indicate the need to match the number of QWs and the total thickness of the active part of the heterostructure with the depth of the e-beam penetration into the structure, which depends on the e-energy, as shown in Figure 3. In this case, it is necessary to take into account the efficiency of carrier transport from barrier layers to quantum wells, which is characterized by the diffusion length of nonequilibrium charge carriers in layers in the (Al,Ga)N system. Known literature data refer to measurements of this parameter, most often in binary GaN layers, using various experimental techniques. Their values vary in the range from 30 nm to 3 μm depending on the structural quality of the layers, which is largely determined by the epitaxy technology used [88–93]. For MOCVD-grown layers on *c*-sapphire substrates, most of the diffusion lengths lie in the range of

Preprints (www.preprints.org) | NOT PEER-REVIEWED | Posted: 20 June 2023 doi:10.20944/preprints202306.1422.v1

100–200 nm. The GaN layers grown on the same substrates using PA MBE have smaller diffusion lengths. For example, in a recent paper by Brandt et al. [92], the diffusion length of carriers for such a layer grown by PA MBE on a MOCVD-grown GaN(0001) template was experimentally determined to be 40±5 nm, and in the work of Daudin's group, this parameter for an $Al_{0.27}Ga_{0.73}N$ layer, also grown by PA MPE on AlN/6H-SiC template, was estimated at 7.5 nm [94].

The next issue discussed in [63] is the dependence of the internal quantum yield on the excitation level, which turned out to be proportional to the e-beam current density. Therefore, based on this dependence, it is desirable to increase this parameter. However, at high values of this parameter, efficient heat removal from the local region of the heterostructure irradiated by an e-beam is problematic. The use of e- beams of small diameter, scanning a sufficiently large area of the structure, makes it possible to simultaneously solve both the problem of heat removal and the problem of a small internal output.

5.1.2. UVC emitters pumped by large-area e-beams generated by CNT-based e-sources

The development of large-area e-sources with CNT-based cathodes, described in section 4.2, allowed the Park group to demonstrate in 2019 the use of such an e-gun for pumping UVC-emitters based on AlGaN heterostructures [65]. Figure 16 shows the main characteristics of a UVC-emitter pumped by such a CNT e-source with an e-beam current of 1.0 mA over an e-irradiation area of 188 mm^2 at an anode voltage of 3 kV. When pumped by this e-source, the MOCVD-grown $Al_{0.47}Ga_{0.53}N/Al_{0.56}Ga_{0.44}N$ structure on a *c*-sapphire substrate exhibited UVC-radiation at 278.7 nm with a maximum output optical power density of 0.11 $mW \cdot cm^{-2}$ (~ 0.3 mW) on a light emitting area of 303 mm^2.

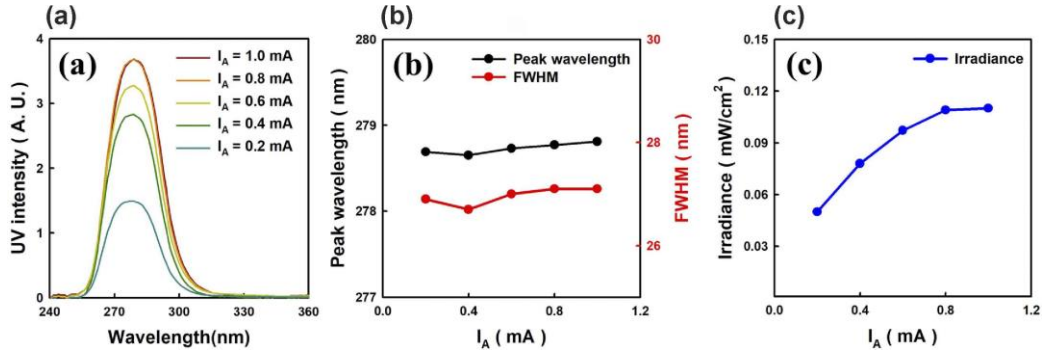

Figure 16. Characteristics of the 5×{$Al_{0.47}Ga_{0.53}N/Al_{0.56}Ga_{0.44}N$:Si} MQW structure with a light emitting area of 303 mm^2: (a) CL-RT spectra measured at a constant energy of 3 keV and various e-beam currents of 0.2 – 1.0 mA; (b) Dependences of the spectral position of the CL peak and its half-width on a e-beam current; (c) Dependence of the output optical power on e-beam current [65].

In the next work of this group [67], an e-source with an arranged array of nanotipped CNT cathodes and an e-emitting area of 276 mm^2 was used to excite an $Al_{0.73}Ga_{0.27}N$(2nm)/AlN(8nm) MQW heterostructure. Figure 17a shows its CL spectra with the main peak at 233 nm, which can be attributed to near-band-edge (NBE) emission. The intensity of this peak increased rapidly as the e-energy increased from 4 to 5 keV, as shown in Figure 17b. The minimum energy of an e-beam for observing MQW-related CL was explained by the presence of a 170-nm-thick Al film on the structure surface, to overcome which the electrons must have sufficient energy (> 3 keV). Simultaneously with the increase in e-energy, the broad peak at about 330 nm became more intense. This peak was attributed to defect states associated with the V_{Al} complexes (V_{Al}-oxygen) of the AlN layer under the upper MQWs [95].

Figures 17b,c show the dependences of the CL intensities on the e-beam parameters, revealing the saturation effect with a maximum power density of 2.3 mW cm^{-2} both with an increase in the e-energy above 5 keV and with an increase in the e-beam current above 0.5 mA. In addition, a weak "red" shift of 37 meV (2nm) for the CL peak spectral position and its widening (not shown) were found with an increase of e-energy. This tendency of AlGaN-based MQWs is opposite to that of the InGaN/GaN MQWs, and can be explained by the thermal effect and composition fluctuations [96–

Preprints (www.preprints.org) | NOT PEER-REVIEWED | Posted: 20 June 2023 doi:10.20944/preprints202306.1422.v1

98]. Namely, the observed effects mean the redistribution of thermally excited electrons into deep localized states, which leads to a red-shift of the CL peak and an increase in its width.

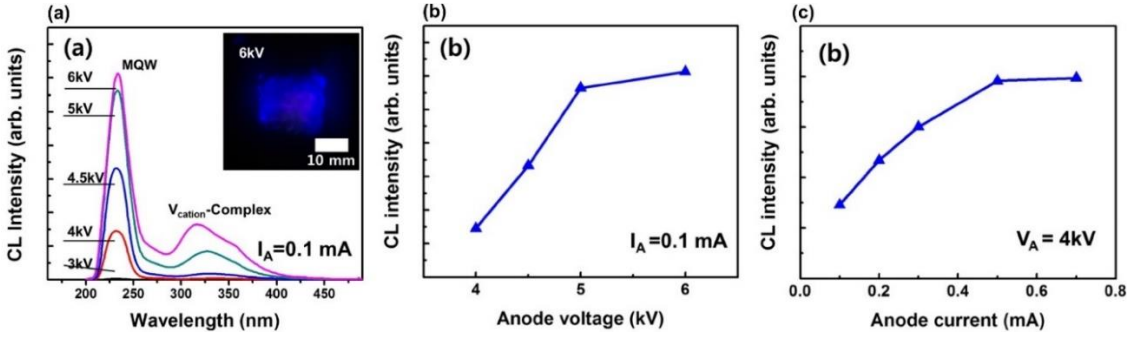

Figure 17. (a) CL spectra of the $Al_{0.73}Ga_{0.27}N$(2nm)/AlN(8nm) MQW heterostructure pumped over an area of 276 mm² at various e-energies in the range of 3 – 6 keV emitted from an e-source with nanotip CNT cathodes. The inset shows a photo of radiation in the visible range. The dependences of the CL-RT intensity on the e-beam energy and the anode current are shown in figures (b) and (c), respectively [67].

5.2. Medium power UVC emitters (up to 1W)

5.2.1. UVC-emitters pumped by thermionic e-guns

All the MQW structures described above were grown by the MOCVD. The first e-beam pumped UVC-emitters with AlGaN-based MQW structures grown using PA MBE were demonstrated in 2015 by Ivanov et al. [99]. A distinctive feature of this work was the method of growing $Al_xGa_{1-x}N$ QWs in the form of $N\times\{(GaN)_m/(Al_yGa_{1-y}N)_n\}$ heterostructures with the introduction of several (N) ultra-thin GaN inserts with a nominal thickness of m monolayers (1ML ~ 0.25nm) into $Al_yGa_{1-y}N$ barrier layers with a nominal distance between GaN inserts of n MLs as proposed by this group in 2009 [100]. The $40\times\{Al_{0.6}Ga_{0.4}N(2.2nm)/Al_{0.7}Ga_{0.3}N(38nm)\}$ MQW structure with the wells grown in the form $3\times\{(GaN)_{0.5}/(Al_{0.7}Ga_{0.3}N)_{3.5}\}$ exhibited UVC radiation at 270 nm and maximum peak (cw-) output optical powers of up to 60(4.7) mW at an WPE of 0.24%, while the internal quantum efficiency of the MQW structure was 50%. The measurement scheme is shown in Figure 2c.

Later, in 2016, Wang's group used this method [101] to fabricate UVC emitters $40\times\{3\times[(GaN)_1/(Al_{0.75}Ga_{0.25}N)_2]/Al_{0.75}Ga_{0.25}N(31nm)\}$ emitting at 285 nm with peak (cw-) output optical powers of 110(25) mW and an maximum WPE of 0.6%, dependences of which on the parameters of e-beams are shown in Figure 18.

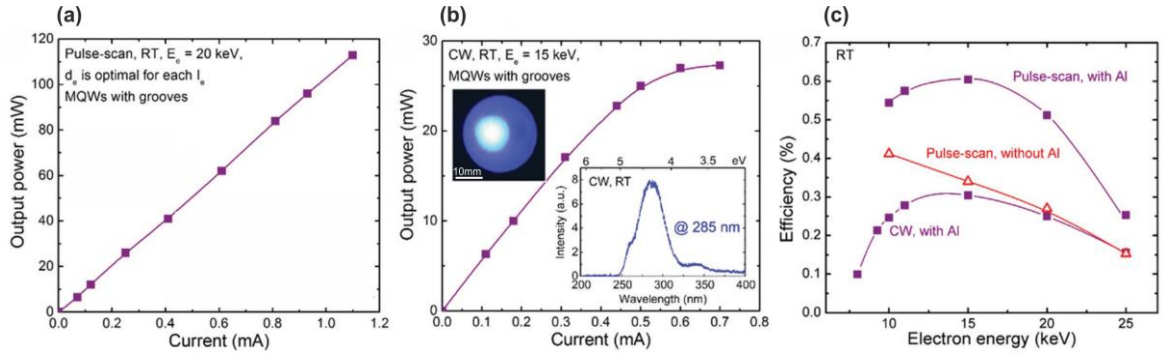

Figure 18. Dependences of the output optical powers of $40\times\{3\times[(GaN)_1/(Al_{0.75}Ga_{0.25}N)_2]/ Al_{0.75}Ga_{0.25}N(31nm)\}$ MQW structure on the e-beam current excited in the pulsed-scan (a) and cw- (b) pumping modes with an e-beam energy of 20 and 15 keV, respectively. The upper inset in (b) shows the emission through paper irradiated by an MQW structure excited by an e-beam with an 8 mm beam spot diameter, and the lower inset shows the CL spectrum. (c) Dependences of the WPE at RT of AlGaN-based UVC emitters on the e-beam energy in different pumping modes [101].

In 2016, Tabataba-Vakili et al. [57] used MOCVD to fabricate $10\times Al_{0.56}Ga_{0.44}N/ Al_{0.9}Ga_{0.1}N$ MQW structures with a well thickness of 1.4 nm. These structures, when pumped by e-beam with an energy of 12 keV, emitted at 246 nm with peak(cw-) maximum output optical powers of 230(30) mW at a

Preprints (www.preprints.org) | NOT PEER-REVIEWED | Posted: 20 June 2023 doi:10.20944/preprints202306.1422.v1

maximum e-beam current of 4.4 mA, as shown in Figure 19a,b. The WPE for the test sample was 0.43% (at 12 keV), and the examination of the several factors contributing to the overall efficiency yielded an estimate for the internal quantum efficiency of about 23%. Moreover, Figure 19c shows the characteristics of the CL spectra excited by an e-beam of different diameters of 3 mm or 50 μm. The lower CL intensity in the case of the focused e-beam was explained by a decrease in the internal quantum yield due to greater heating of the active region by an e-beam of smaller diameter. However, this explanation does not seem to be convincing, since linear dependences of the output optical powers on the e-beam currents were observed for both e-beam diameters.

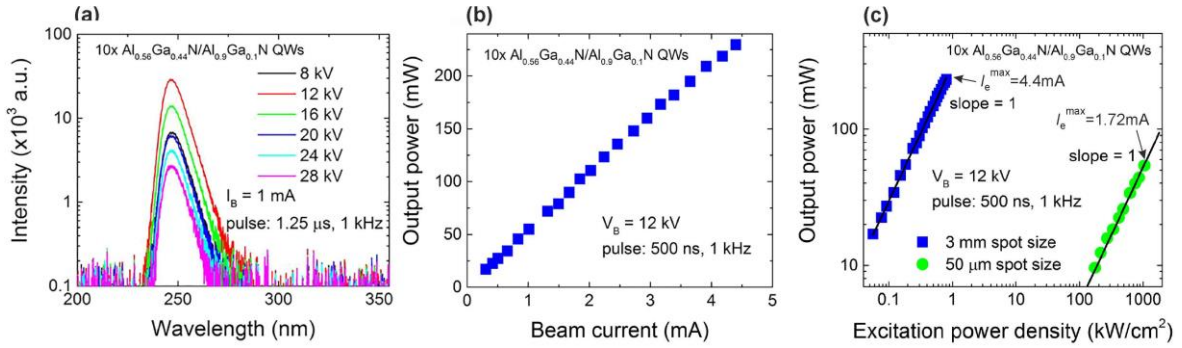

Figure 19. (a) CL-RT spectra of the 10×{$Al_{0.56}Ga_{0.44}N/Al_{0.9}Ga_{0.1}N$} MQW structure, measured at e-beam energies varied from 8 to 28 keV and an e-beam current of 1 mA with a pump pulse duration of 1.25 μs and a frequency steps 1 kHz. (b) Dependence of the output optical power on the pump current by electrons with an energy of 12 keV, a pulse duration of 500 ns, and a repetition rate of 1 kHz. (c) Comparison in a double-logarithmic plot of the CL output power vs. e-beam excitation power density for the incident e-beam diameters of 3 mm and 50 μm [57].

The next step in the development of e-beam pumped UVC emitters was the transition to the use in them of light-emitting N×{GaN_m/AlN_n} MQWs heterostructures with monolayer (1ML~0.25 nm) and even fractional thicknesses of the wells. The possibility of efficient light emission by such structures in the UV range was theoretically substantiated in 2011 by Kamiya et al. [102], and almost immediately implemented by Taniyasu and Kasu using MOCVD technology [103]. Later in 2016, such MQW structures were grown by Jena's group using PA MBE technology [104]. They used either standard or modified Stranski–Krastanov growth modes under N-rich conditions ($Ga/N_2^* < 1$) to induce formation of 3D-dimensional GaN islands (dots = disks) into GaN QWs with nominal thicknesses of 1–3 MLs. Despite the enhanced photoluminescence, IQE and TE-polarization of the output emission from these heterostructures, the maximum achieved output power density of the related UVC LEDs at the shortest wavelength of 234 nm was below 0.4 mW·cm^{-2} [105]. A detailed analysis of the properties and fabrication technologies of ML-thick GaN/AlN MQWs and related UV light-emitting devices was recently made in review [54].

The first ML-thick GaN/AlN MQW structures for e-beam pumping with a number of periods from 40 to 360 (with a total structure thickness of ~1.8 μm) were grown using PA MBE in 2018 [106]. The main distinguishing feature of their fabrication was the use of metal-enriched conditions for growth of both barrier layers and quantum wells with typical flux ratios of Al/N_2^*~1.1 and Ga/N_2^* up to 2.2 at relatively low substrate temperatures of 690-700°C, as shown in Figure 20a.

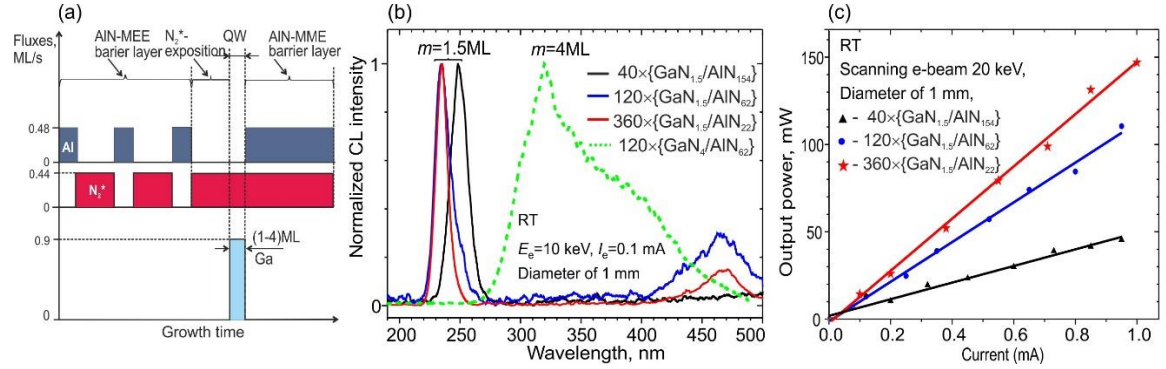

Preprints (www.preprints.org) | NOT PEER-REVIEWED | Posted: 20 June 2023 doi:10.20944/preprints202306.1422.v1

Figure 20. (a) Typical shutter sequence during the growth of a GaN/AlN QW with a various well thickness determined by the Ga-exposure time. (b) Normalized RT CL spectra of the N×{$GaN_{1.5}/AlN_m$} MQW structures with N = 40 − 360 and m = 22 − 154, measured at E_e = 10 keV, I_e = 0.1 mA, and beam spot diameter of ~1 mm. (c) Peak output power as a function of the e-current of the pulse-scanning e-beam with E_e = 20 keV, measured at RT for the MQW structures [106].

During the growth of structures, excess Al was consumed due to short-term exposures of the surface under plasma-activated nitrogen flux before the growth of each QW, and excess Ga evaporated during the subsequent growth of barrier layers, since the growth temperature provided a rather high Ga evaporation rate of 0.2 – 0.3 ML s^{-1} [107].

The used Me-rich conditions at low growth temperature make it possible to achieve very sharp interfaces in ML-thick QWs due to the kinetic limitation of the Ga segregation effect in the heterostructure, which plays a significant role at higher temperatures. Second, these conditions ensured the precise control of the nominal thicknesses of both QWs and barrier layers using calibrated data on N_2*-flux [107]. The sharpness of the symmetrical interfaces in the MQW structures and accuracy of setting their parameters were confirmed using images from high-angle annular dark field scanning transmission electron microscope (HAADF STEM) and high-resolution x-ray diffraction (HRXRD) ω-2θ scans of (0002) symmetric reflection [106].

Figure 20b demonstrates narrow CL peaks with a spectral width of ~ 20 nm in the UVC range of 235 – 250 nm for N×{$GaN_{1.5}/AlN_m$} MQW structures with N=40 – 360 and m=22 – 154, excited by a thermionic e-gun with electron energy 20 keV. From them, linear dependences of the output peak optical power on the pump current follow, and its maximum values of 150 mW are achieved at a pulse-scanning mode with e-current of 1 mA of the structure with the largest number of QWs, as shown in Figure 20c. At the same time, the maximum WPE value of 0.75% is also observed in this structure. The maximum cw-output power in this structure reached 28 mW when it was excited by an e-beam with E_e = 15 keV and a diameter of 10 mm at a e-current of 0.45 mA (i.e. WPE was 0.4% in this excitation mode).

In 2019, the Monroy group launched a series of works on the development of e-beam pumped UVC and UVB emitters based on AlGaN/AlN MQW structures grown using PA MBE [108–110]. In the first works [108,109], nanowire structures were grown starting with the growth of base GaN nanowires with a height of 900 nm, followed by 88×{$Al_xGa_{1-x}N$(x = 0, 0.05, 0.1)/AlN} MQWs having a well thickness of 0.65 – 1.5 nm, while the barrier thickness exceeded 3 nm. All parts of nanowires were grown under the same N-rich conditions with a flux ratio Ga/N_2* of 0.25 at a substrate temperature of 810°C, and a growth rate of 330 nm·h^{-1}. Figure 21a and 21b show transverse and plan-view images of these structures obtained using a scanning electron microscope (SEM), which indicates the formation of separate nanocolumns with a surface density 6 – 8×10^9 cm^{-2} and a diameter of 30 – 50 nm.

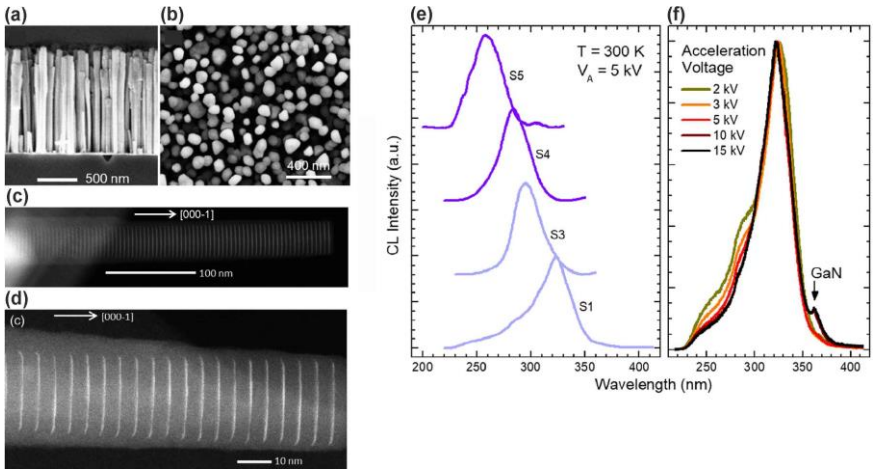

Figure 21. Cross-section (a) and plan-view (b) SEM images of a nanowire structure with MQW 88×{$Al_{0.1}Ga_{0.9}N$/AlN} [108]. HAADF STEM images of dispersed NWs containing 88×{GaN(1.5nm)/AlN(3nm)} (c), 88×{($Al_{0.1}Ga_{0.9}N$)(0.65nm)/ AlN(3.85nm)} (d). (e) Normalized CL-RT spectra for the following structures: S1: 88×{GaN(1.5nm)/AlN(3.0nm)}; S3: 88×{GaN(0.75nm)/AlN(3.75nm)}; S4: 88×{($Al_{0.1}Ga_{0.9}N$)(0.75nm)

Preprints (www.preprints.org) | NOT PEER-REVIEWED | Posted: 20 June 2023 doi:10.20944/preprints202306.1422.v1

/AlN(3.75nm)}; S5: 88×{($Al_{0.1}Ga_{0.9}N$)(0.65nm)/AlN(3.85nm)}. For clarity, the spectra are shifted vertically [108]. (f) Normalized CL spectra of the MQW structure S4: 88×{($Al_{0.1}Ga_{0.9}N$)(0.75nm)/AlN(3.75nm)}, measured at various electron energies from 2 to 15 kV. The CL peak associated with the emission from GaN in the bases of nanocolumns is observed only at an accelerating voltage above 5 kV [108].

Figures 21c,d showing HAADF STEM images of individual QWs confirmed the given values of layer thicknesses and periods of MQW structures. The latter parameter was also confirmed by XRD analysis (not shown). Finally, in Figures 21e,f show the CL spectra of these structures measured at RT, which revealed approximately the same shape of one peak, the position of which shifted from 260 to 340 nm with an increase in the QW thickness from 0.65 to 1.5 nm (from 2.5 to 6 ML) respectively.

The ratio of the integrated luminescence intensity at RT and at low temperature was used to estimate the internal quantum efficiency (IQE) of these structures. The measurements of PL and CL spectra revealed IQE = 63% for the structure emitting at 340 nm, and it decreases to ≅ 22% for the structure, emitting at 258 nm.

In the next work [110], this group studied planar superlattice (SL) heterostructures with $Al_xGa_{1-x}N$/AlN (x = 0 or 0.1) quantum dots (QDs) with a density >10^{11} cm^{-2} grown by PA MBE with a total thickness of 530 nm (100 periods) on 1 μm thick (0001)-oriented AlN-on sapphire templates at a substrate temperature of 720°C. The growth of GaN and $Al_{0.1}Ga_{0.9}N$ QDs was carried out under nitrogen-enriched conditions with different flux ratios Ga/N = 0.29 - 0.85, while for the growth of barrier layers with a thickness of 4 nm, on the contrary, slightly metal-enriched conditions were used with the flux ratio Al/N=1.1.

All structures exhibited AFM images with a relatively smooth surface topography of the structures, as shown in Figure 22a. However, HAADF images of the QWs in these SLs demonstrated an inhomogeneous distribution of their thicknesses with the formation of local small extensions in the form of QDs, shown in Figure 22b-d. Such an inhomogeneous QW/QD topography can be associated with nitrogen-enriched growth conditions used during QD growth, when their nominal thickness was proportional to the Ga flux. Therefore, observed in Figure 21e, the short-wavelength shift of the CL-RT peaks from 335 to 244 nm with a decrease in the Ga flux can be caused by a decrease in nominal thickness of the QDs and a corresponding decrease in their average size. A blue shift is observed in the peak emission wavelengths of $Al_{0.1}Ga_{0.9}N$ dots as compared to GaN dots with the same Ga-flux. The shift corresponds to an average increase of 250 meV in band gap, which is consistent with the incorporation of 10% of Al in the dots.

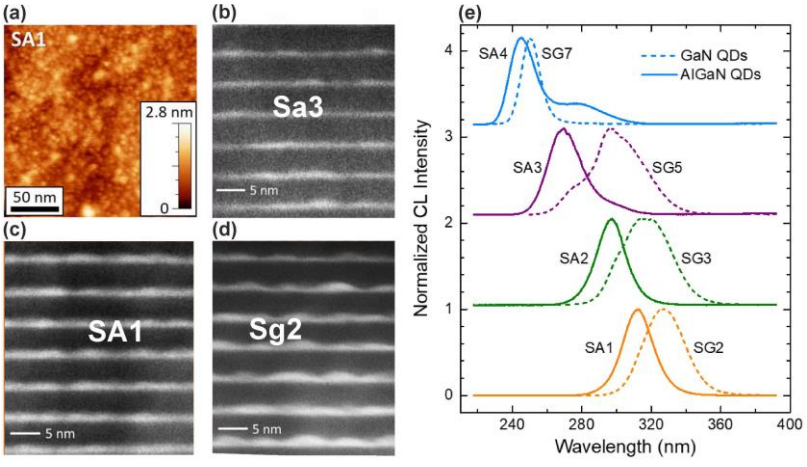

Figure 22. (a) AFM image of the surface of the 100×{($Al_{0.1}Ga_{0.9}N)_5$/AlN(~ 2 nm)} structure. HAADF STEM images of the following MQW structures: SA3:100×{($Al_{0.1}Ga_{0.9}N)_{2.9}$/AlN(~ 2 nm)} (b), SA1: 100×{($Al_{0.1}Ga_{0.9}N)_5$/AlN(~ 2 nm)} (c) and SG2: 100×{$GaN_{4.6}$/AlN(~ 2 nm)} (d). These structures were grown under nitrogen-enriched conditions with flux ratios III/N = 0.47(SA3), 0.8(SA1), and 0.73(SG2). (e) Normalized CL-RT spectra for GaN/AlN (SG) (dashed lines) and $Al_{0.1}Ga_{0.9}N$/AlN (SA) (solid lines) MQW structures grown with various m and Ga fluxes: SA4, SG7 – m = 1.8-2.0 ML, Ga = 0.149 ML/s; SA3, SG5 – m = 2.6-2.9 ML, Ga = 0.220 ML/s; SA2, SG3 – m = 3.8-4.2 ML, Ga = 0.319 ML/s and SA1, SG2- m = 4.6-5 ML, Ga = 0.38 ML/s (from top to bottom respectively) [110].

Preprints (www.preprints.org) | NOT PEER-REVIEWED | Posted: 20 June 2023 doi:10.20944/preprints202306.1422.v1

It is important that the internal quantum efficiency of UVC-emitters with GaN(or $Al_{0.1}Ga_{0.9}N$)/AlN QDs, which was estimated in the first approximation from the ratio of the PL intensities at room and zero (extrapolated) temperatures, was 50% for the structures grown at the highly nitrogen-enriched conditions with flux ratio $Ga/N_2^* < 0.75$. It should also be noted that such a high efficiency was observed in a wide range of power densities of PL laser excitation up to 200 $kW \cdot cm^{-2}$. In addition, the same spectral position of the main CL peak was shown with an increase in the pumping electron energy, as shown in Figure 23a. However, it should be noted that at energies above 20 keV, an additional long-wavelength peak appeared at 340 nm, which was associated with the penetration of a high-energy e-beam into the AlN buffer layer, in which it excites defective radiation (associated with carbon atoms and other defects).

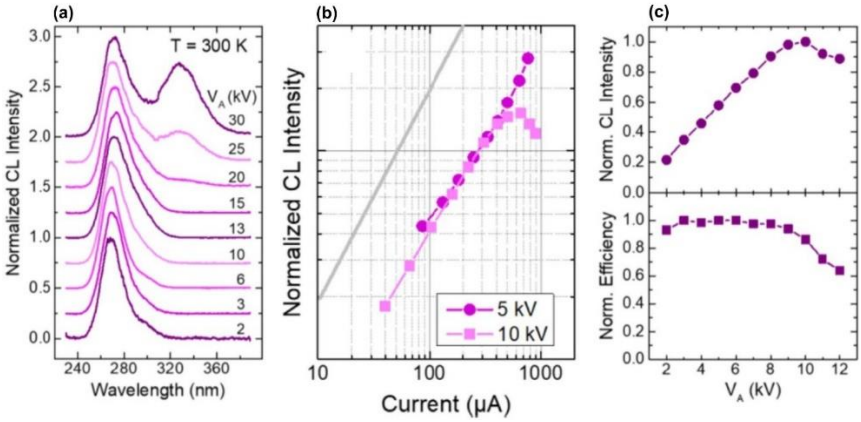

Figure 23. (a) Normalized CL spectra of the 100×{($Al_{0.1}Ga_{0.9}N)_{2.9}$/AlN(~2nm)} MQW structure, excited at various e-beam energy. (b) Variation of CL intensity as a function of the injection current measured for the same sample at E_e = 5 keV and 10 keV. The slope of the solid grey line corresponds to a linear increase. No saturation is observed up until 800 μA for E_e = 5 keV while a saturation for currents higher than 400 μA is observed at E_e = 10 keV. (c) Normalized CL intensity (upper curve) and emission efficiency (lower curve) as a function of an anode voltage for the same sample. Measurements were performed using an e-gun operated in direct current mode, under normal incidence, with a beam spot diameter of 4 ± 1 mm [110].

Figure 23b demonstrates an almost linear increase in CL intensity as the e-energy increases to 10 keV, which was explained by a simple increase in the active (light emitting) region in the structures at constant excitation efficiency, as shown in Figure 23c. The CL intensity began to fall at electron energies above 10 keV, which was accompanied by a drop in efficiency. This effect was explained by the penetration of the exciting beam into the substrate and the charging of dielectric AlN. Finally, a linear increase in CL intensity was observed up to the maximum possible e-beam current up to 0.8 mA for both low and medium e-energies. However, at a higher electron energy (~10 keV), this dependence demonstrated the saturation effect at high e-currents, which was also explained by the surface charging. Unfortunately, these papers did not report on the absolute values of the output optical powers from the studied heterostructures.

Recently (in 2023), two research groups using PA MBE technology have joined the study of ML-thick GaN/AlN MQW structures emitting in the UVC range with e-beam pumping. The first of them, headed by Daudin, is the leading scientific groups that have developed the basic understanding of the PA MBE growth kinetics of III-N layers and associated heterostructures [111,112]. In particular, since the late 1990s, they have been studying the features of the growth of GaN/AlN heterostructures, but so far their main attention has been focused on the formation of quantum dots in this system according to the Stranski-Krastanov mechanism, the radiation of which is outside the UVC range. This group was the first to measure the critical thickness of 2ML for the 2D-3D transition during the growth of GaN over AlN [113]. In addition, they carried out pioneering studies of segregation phenomena during the growth of GaN/AlN heterostructures, which determine the temperature dependences of the sharpness and symmetry of heterointerfaces in these structures [114]. In a recent work of this group [115], the fine structure of the CL spectra of GaN disks 1–4 ML thick in AlN nanowires was studied in order to control the emission wavelength of AlN nanowires. Particular attention in this work was paid to emission lines below 240 nm (which corresponds to 1 ML), which

Preprints (www.preprints.org) | NOT PEER-REVIEWED | Posted: 20 June 2023 doi:10.20944/preprints202306.1422.v1

were assigned to the recombination of confined carriers in the incomplete QWs with a lateral size smaller or comparable to the 2.8 nm GaN Bohr exciton radius. Their emission consists of sharp lines extending up to 215 nm near the edge of the AlN band, as shown in Figure 24.

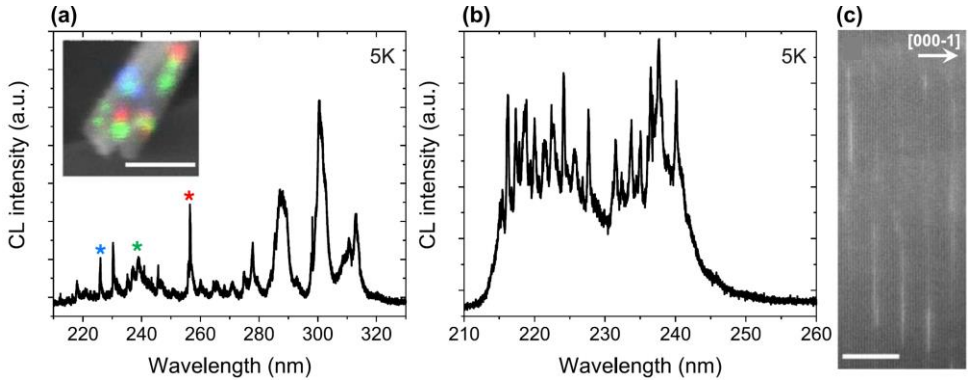

Figure 24. (a) 5K CL spectrum of two single NWs with a GaN/AlN SL with different thicknesses of QWs. The inset shows CL emission with color code referring to different spots emitting at different wavelengths. The peak at 240 nm is assigned to 1 ML thick GaN QWs. The scale bar in the inset is 200 nm. (b) 5K CL spectrum in another spot, emphasizing the presence of sharp lines below 240 nm, which are assigned to the presence of incomplete QWs. (c) STEM-HAADF image of the incomplete GaN QWs. The scale bar is 5 nm [115].

The RT-CL intensity of an ensemble of GaN quantum disks embedded in AlN nanowires is about 20% of the low temperature value, emphasizing the potential of ultrathin/incomplete GaN quantum disks for deep UV emission. The GaN/AlN MQWs were grown by alternated exposure to metal and nitrogen fluxes at the relatively high growth temperature of 750 – 800°C, allowing eased metal diffusion on the top surface prior to nitridation of the metallic layer.

In contrast, Araki's group grew a GaN/AlN superlattice with a well thickness estimated at 1.1-1.4ML using PA MBE with metal-rich growth conditions for both group III atoms, which provided atomically flat AlN surface and abrupt interfaces in these heterostructures [116]. Subsequently, excess metals were eliminated by so-called method of droplet elimination by radical beam irradiation for AlN (originally this method was developed by this group for InN [117]) and growth interruptions for GaN. These superlattices exhibited CL spectra with a peak wavelength of 230–260 nm at RT, as expected. The emission wavelength shifted with increasing thickness of the AlN layer.

5.2.2. Sub-Watt power UV-emitters cw-pumped by large-area CNT-based e-sources

The possibility of exciting UV-emission from a k-modification sapphire plate (k-Al_2O_3) was initially demonstrated in 2020 by Park's group using large-area e-sources based on a cold field CNT cathode shown in Figure 2e [56]. Fully vertical aligned cone-shaped CNT emitters are arranged periodically at 30 μm intervals to enhance the electron emission current. The one island consists of 49 CNT emitters in the square shape. These islands are patterned at 0.5 mm intervals to reduce cathode current leakage through the gate electrode.

Figure 25a shows that the CL spectra of this plate exhibited several lines in a wide spectral range above 200 – 400 nm at low electron energies (5 – 9 keV), but at high electron energies (10 keV) only one main broad peak at 226 nm is observed. The output optical power, integrated over the spectrum and emitting area of 960 mm^2, was 113 mW at a WPE of 0.87%. However, the very wide emission spectrum of such a UV emitter up to the visible range limits its application.

Preprints (www.preprints.org) | NOT PEER-REVIEWED | Posted: 20 June 2023 doi:10.20944/preprints202306.1422.v1

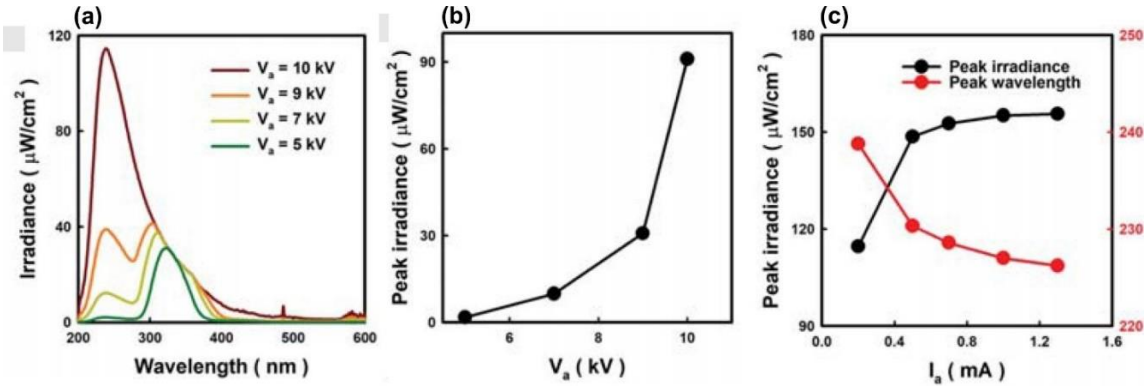

Figure 25. (a) Spectral density of output CL power from k-sapphire excited by e-beams with various electron energy in a range of 5-10 keV, (b) dependence of the peak density of output optical power on the anode voltage (e-beam energy), (c) dependences of the CL peak spectral position and density of output peak optical power on an anode current [56].

In another paper published in 2021, Mohan et al. [68] used a large-area CNT e-emitter, shown in Figure 9, in the development of UVA emitters based on GaN/AlGaN MQW structures. Figure 26 shows the CL spectra and the dependence of the output power on the pumping current for a UVA-emitter based on a 18×{GaN(2.1 nm)/AlGaN(9 nm)} MQW structure emitting at 330 nm. The defect luminescence (< 10%) in the visible region constitutes the well-defined quality of the MQWs AlGaN/GaN grown on AlN/sapphire substrate. When it was pumped in a cw-mode by an e-beam with energy of 7 keV and a maximum current of 1 mA, a maximum output optical power of 225 mW was achieved with an as-calculated quantum efficiency of 3.6%.

DC-operated triode UV-emitter does not require pulse conditions and can be easy operational with minimal power setup arrangements. They are compact, straightforward, and easy to use and control, requiring low maintenance and better efficiency.

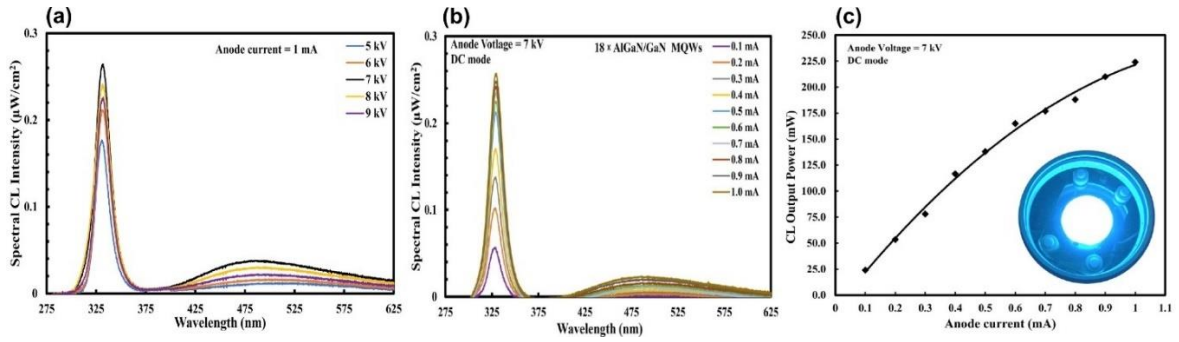

Figure 26. CL-RT spectra of a 18×{GaN(2.1 nm)/AlGaN(9 nm)} MQW structure, measured at various e-beam energies (a) and currents (b). (c) Dependence of the CL output power from this structure on the e-beam current at an anode voltage of 7 kV. The inset shows a photo captured during actual UV – CL emission from the 2-inch AlGaN/GaN MQW wafer at an anode voltage of 7 kV and anode current 1 mA under the DC electric field [68].

The successful development of an UVC-emitter pumped by a large-area (2 inches) CNT e-source and increased WPE was recently demonstrated by Wang et al. from Peking University [118]. They proposed a specially designed new type of ML-thick GaN/AlGaN/AlN MQW structures. The main distinguished feature of these emitters is a new QW design, in which a 2-ML-thick $Al_xGa_{1-x}N$ layer is introduced before one-ML thick GaN QWs according to the formula $100\times\{GaN_1/(Al_xGa_{1-x}N)_2/AlN_{40}\}$ (x = 0.6, 0.5, 0), as shown in the inset in Figure 27a.

The authors calculated that the maximum overlap degree of the wavefunctions of electrons and holes in such complex QWs is reached at x = 0.6 and amounts to 0.85. Figure 27a confirms this theoretical result by showing the CL spectra of three different MOCVD-grown MQW structures and revealing the highest CL intensity for the proposed optimal design. Importantly, this structure emits at 248 nm with output optical power controlled by both anode voltage and e-current, as shown in Figure 27b,c.

Preprints (www.preprints.org) | NOT PEER-REVIEWED | Posted: 20 June 2023 doi:10.20944/preprints202306.1422.v1

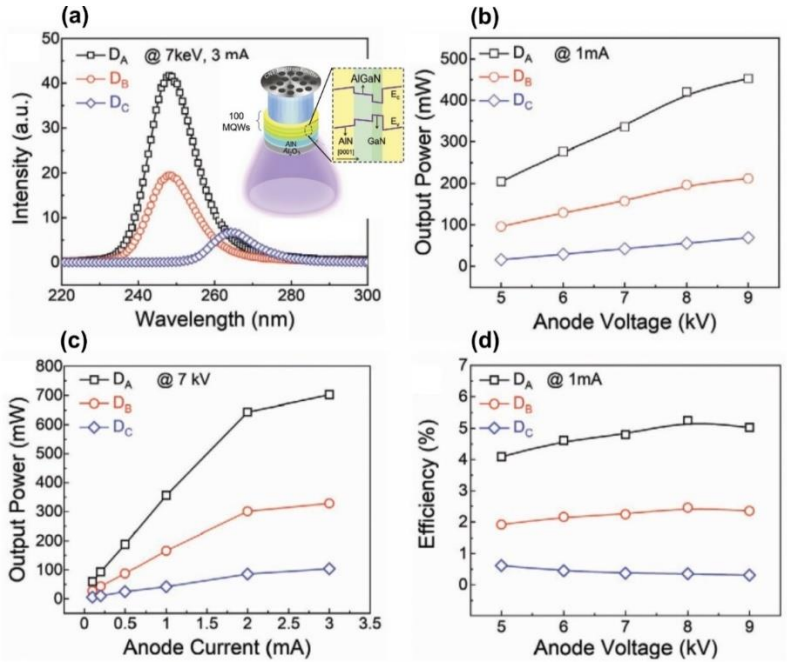

Figure 27. (a) CL spectra of three MQW structures 100×{$GaN_1/(Al_xGa_{1-x}N)_2/AlN_{40}$} with various Al –content in 2ML-thick $Al_xGa_{1-x}N$ layer: x = 0.6(D_A), 0.5(D_B), 0(D_C) . Dependences of the output power of these three structures on the anode voltage (b) and anode current (c). (d) Dependences of the WPE on the anode voltage for these three structures [118].

A maximum power value of 702 mW was achieved at an anode voltage of 7 keV and an anode current of 3 mA. However, Figure 27d shows that the maximum value of the WPE equal to 5.2% was observed at a lower current of 1 mA and the same anode voltage, corresponding to an output power of about 300 mW. Note that this WPE value is more than five times higher than the best values of this parameter for sub-250 nm UVC LEDs.

5.3. High power (up to several tens of Watt) pulsed UVC emitters

A Watt-level for output peak optical power for electron-beam-pumped UVC emitters was overcome in 2019 by Wang et al. [119]. This group was the first to transfer the idea of ML-thick N×{GaN_m/AlN_n} MQWs structures (m = 1 − 3) from PA MBE to MOCVD technology and used to pump these heterostructures with relatively high-current (up to 40 mA) pulsed thermionic e-guns with LaB_6 cathodes. Figure 28a shows high-resolution X-ray diffraction (HRXRD) 2θ-ω scans along symmetric (0002) plane, which revealed more than 14 satellite peaks, indicating satisfactory periodicity and sharp interfaces in the MQW structures. Their simulation confirmed the barrier thickness of about ≈10.2 nm, and the well width of ≈0.3, 0.45, and 0.72 nm, being in good agreement with the designed values 1,2 and 3 ML, respectively. An atomic force microscopy (AFM) study of the surface topography of these structures showed distinct atomic steps on the surface with a typical RMS surface roughness (RMS) of 0.32 nm in a 3 × 3 μm^2 scan area, as shown in Figure 28b. Moreover, Figure 28c shows HAADF measurements of the MQW structures with different nominal QW thicknesses, which are recognized by the bright stripes, although a slight interdiffusion can be seen in the TEM images between the well and top barrier layers. This is mainly caused by the relatively high growth temperature by MOCVD. The well thicknesses for the three samples are one to two MLs, two to three MLs, and three to four MLs, which is in good accord with the XRD results.

Preprints (www.preprints.org) | NOT PEER-REVIEWED | Posted: 20 June 2023 doi:10.20944/preprints202306.1422.v1

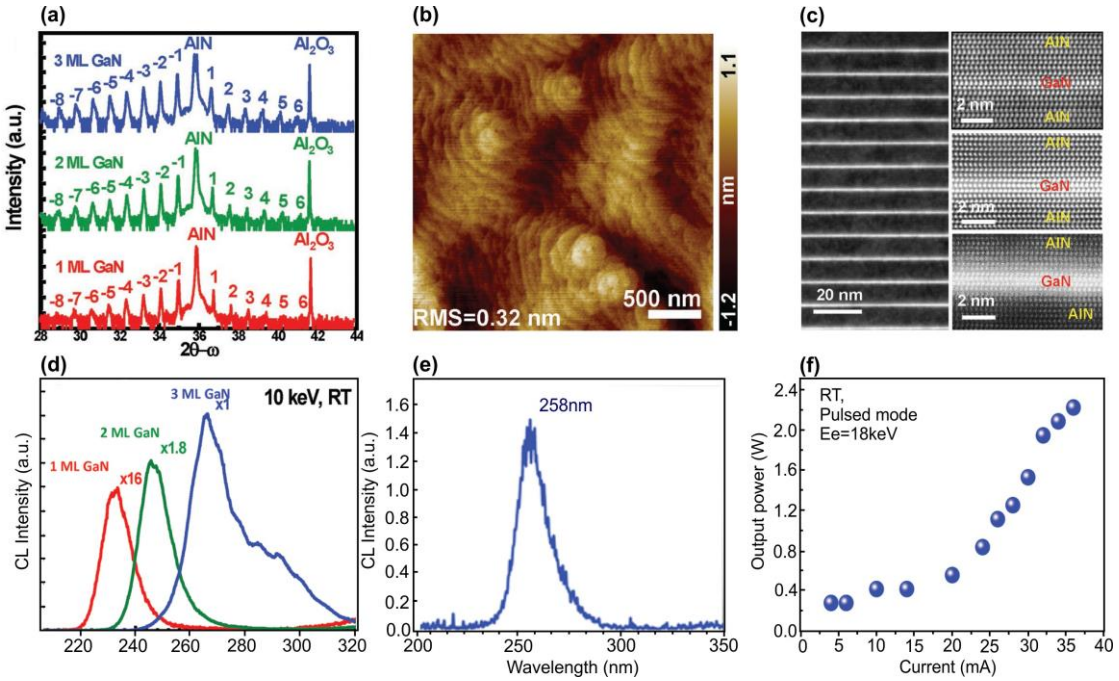

Figure 28. (a) XRD ω-2θ scans of symmetric (0002) plane for samples with one ML GaN well (red line), two MLs GaN wells (green line), and three MLs GaN wells (blue line). (b) AFM image taken in a scanned area of 3 × 3 μm² with an RMS value of 0.32 nm. (c) Cross-sectional HAADF-STEM images in the region of several periods of nominal one ML GaN (left) and one period of one, two, and three MLs GaN well (right). (d) CL spectra of 100×{GaN_m/AlN_{40}} MQW structures with different nominal well thicknesses (m=1,2,3) grown with MOCVD. (e) CL spectrum of the 150×{GaN_2/AlN_{40}} MQW structure with optimized parameters (f) and its output optical power via the e-current supplied by a e-gun with a LaB_6 thermionic cathode operated in a pulsed mode [119].

The MOCVD-grown structures with nominal QW thicknesses varying from 1 to 3 ML exhibited CL in the range of 230 to 270 nm, as shown in Figure 28d. It is important that the intensity of the short-wavelength CL was more than an order of magnitude lower than the intensity of the long-wavelength CL. After optimization of the design of such UVC-emitters, a 150×{GaN_2/AlN_{40}} MQW structure was grown, which demonstrated CL single peak at 258 nm with a maximum pulsed optical power of up to 2 W at an e-beam supplying by an e-gun with LaB_6–cathode, which provided e-beam current of 37 mA and energy of 18 keV, as shown in Figure 28e,f.

At the same time, the development of PA MBE to obtain ML-thick MQWs continued, and the results on growing a large series of such structures with different QW thicknesses and growth conditions were published in 2021 − 2023 in [120,121]. Features of the growth of PA MBE AlN/c-Al_2O_3 templates for these structures, including the issues of reducing the density of threading dislocations in these templates to ~$5 \cdot 10^{9}$ cm^{-2} and the development of elastic stresses in them, are described in [122,123]. Figure 29a shows the first CL spectra of these samples with a QW thickness m = 1.25 − 7 MC [120].

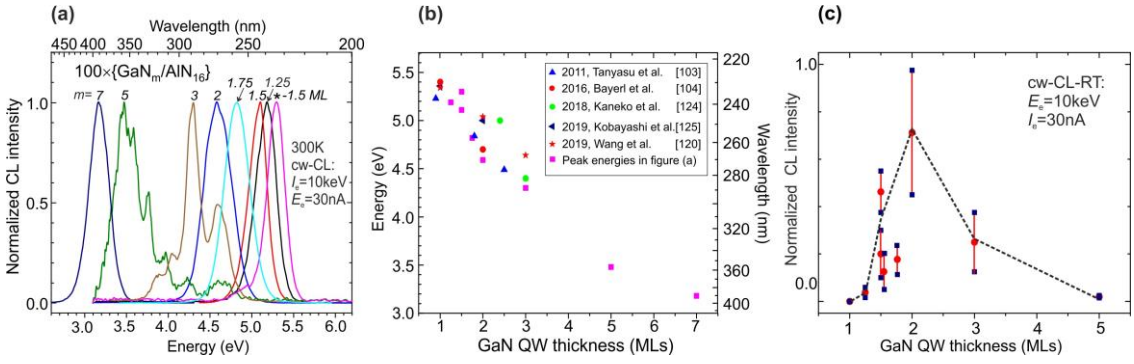

Figure 29. (a) Normalized CL-RT spectra of N×{GaN_m/AlN_{16}} MQW structures, measured at e-beam energy and current of 10 keV and 30 nA, respectively. Structure grown at m = 7 ML had N = 25, while all others were grown with N=100. All structures were grown in one series as described in [120]. The spectrum marked by «*»

Preprints (www.preprints.org) | NOT PEER-REVIEWED | Posted: 20 June 2023 doi:10.20944/preprints202306.1422.v1

was measured for the structure grown at m = 1.5 ML, n = 22 ML, and N = 120 as described in [106]. (b) dependence of the CL peak energy positions on the nominal QW thickness in MQW structures in (a) and described in [103,104,106,120,124,125]. (c) Dependence of the CL intensity on the QW thickness in the MQW structures whose spectra are shown in (a) [120].

Topography studies of the 350×{$GaN_{1.5}/AlN_{16}$} structures grown at the Me-rich conditions revealed signs of spiral growth with the formation of a terrace-like surface with steps 1 − 2 ML height and a width (inter-step spacing) ~20 nm, as shown in Figure 30a,b. Despite the formation of a surface with nanohillock topography, its root-mean-square roughness was 0.3 − 0.7 nm and its values weakly depended on the AFM scanning area, which varied from 1 × 1 μm² to 5 × 5 μm². The main factor influencing the surface roughness was the value of the Ga/N_2* flux ratio used during QW growth. During QW growth under weakly metal-enriched conditions with Ga/N_2* ~ 1.1, the surface corresponded to a mixed growth mechanism with signs of both a step-flow and 2D nucleation growth mechanisms, which led to the formation of a surface with a characteristic step height of 1 ML and minimum values of rms 0.3 nm (see Figure 30a). In the case of a high value Ga/N_2* ~ 2), the surface to a greater extent corresponded to the step-flow growth mechanism with the formation of steps with a height of 2 ML, as shown in the inset of Figure 30b. Moreover, growth of QWs under N-rich conditions corresponded to the Ga/N_2* = 0.6 the surface exhibited the roughest 3D-surface topography without any evidence of the stepped topography (see Figure 4c,d in [121).

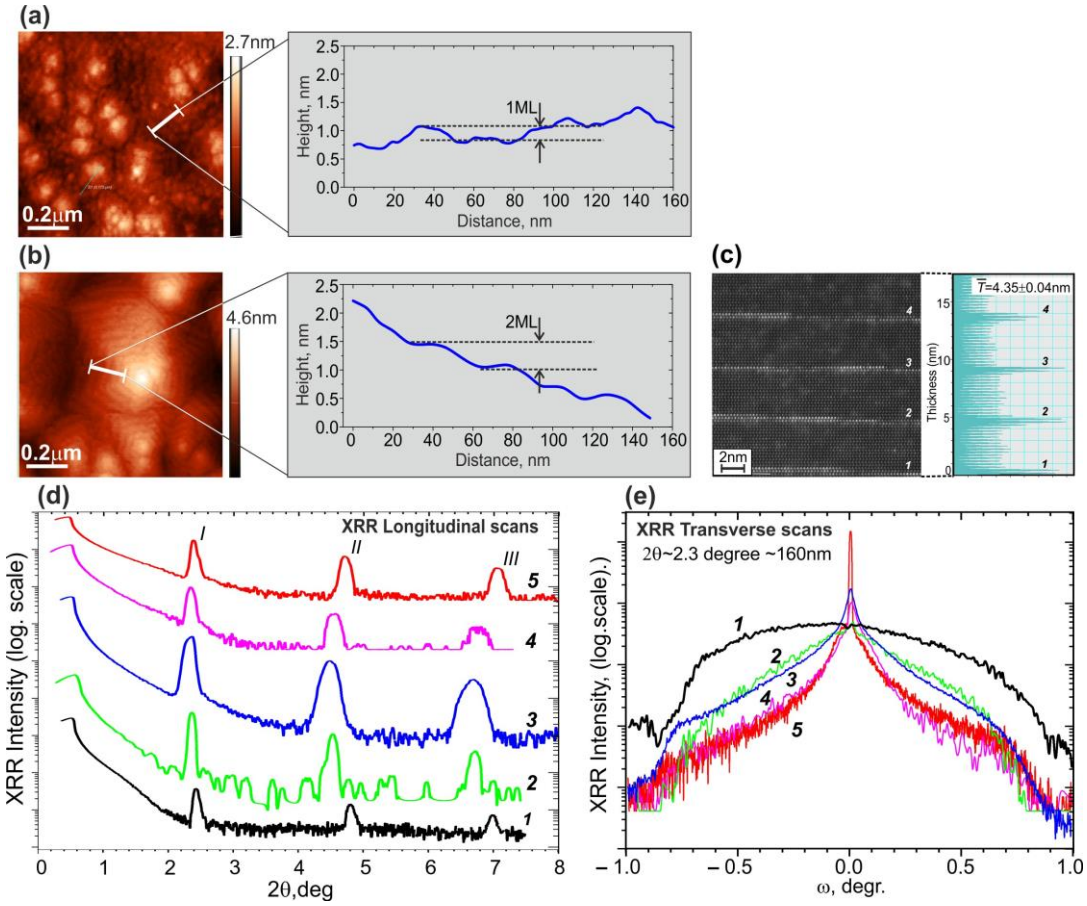

Figure 30. AFM images of the surfaces of 400×{$GaN_{1.5}/AlN_{16}$} MQW structures with QWs grown at Ga/N_2* ratios of 1.1 (a) and 2.2 (b). Insets in the figures depict changes in the profile height along the white line segments plotted on these figures. (c) Cross-sectional HAADF STEM image of the 100×{$GaN_{1.5}/AlN_{16}$} MQW structure with QWs grown at Ga/N_2* of 2.2. The inset shows integrated brightness distribution in the vertical direction. The longitudinal (Bragg-like) 2θ- (d) and transverse ω- (e) scans of X-ray reflectivity curves of 400×{GaN_m/AlN_{16}} MQW structures with various nominal well thickness m: (*1*: m = 1.2; (*2* −*5*): m = 1.5) grown at different Ga/N_2* flux ratio on different AlN/*c*-Al_2O_3 templates: *1*: Ga/N_2* = 0.6 on PA MBE-AlN template; *2,3*: Ga/N_2* = 2.2, *4,5*: Ga/N_2* = 1.1; *3,4* – on AlN-PA MBE templates and *2,5* – on double MOCVD/PAMBE ones [121].

 doi:10.20944/preprints202306.1422.v1

Figure 30c shows a HAADF STEM image of the internal morphology of one of the MQW structure grown at $Ga/N_2^* = 2.2$, which confirms, first, the nominal period of this structure [121]. In addition, this image corresponds to the AFM image of the surface and indicates the formation of stepped cross-section profiles of the QWs with regions of different thicknesses, both 1 and 2 ML, which corresponds to their fractional (1.5 ML) nominal thickness.

Studies of the structures using HRXRD with scanning of the symmetric reflection (0002) also confirmed the nominal values of the MQW parameters of the structures [120,121]. However, measurements of longitudinal and transverse scans of X-ray reflection curves (XRR), which are shown in Figure 30d,e, respectively, turned out to be much more informative for the characterization of QWs. These scans confirmed the smoothest morphology of both the surface and QWs in structures grown under weak metal-enriched conditions ($Ga/N_2^* = 1.1$) according to a mixed growth mechanism with minimal AFM roughness and a characteristic step height of 1 ML. The higher surface and QW roughness found for the structures grown at $Ga/N_2^* = 2.2$ was also consistent with the AFM measurement data. And, finally, the roughest morphology was found in structures with QWs grown under nitrogen-enriched conditions ($Ga/N_2^* = 0.6$) that corresponds to AFM data described above.

The CL спектры in these heterostructures were excited using various high-current e-guns. Initial studies were carried out using a thermionic e-gun with a LaB_6-based cathode emitting an e-beam with a diameter of ~1 mm and a maximum pulsed e-current of up to 60 mA current with a pulse duration of about 50 ns [120]. In addition, in both works an e-gun with cold plasma cathode based on a surface discharge on a ferroelectric surface was used, which supplied the emission of e-beams 4 mm in diameter with maximum currents up to 500 mA [120] and 2.0 A [121]. Figure 31a shows two CL spectra of the $360\times\{GaN_{1.5}/AlN_{22}\}$ structure measured using these types of e-guns for their excitation. Both spectra exhibit single peaks at 241 − 242nm with half-widths of 12 − 13 nm. The peak intensity of the output optical power of the CL excited by the LaB_6-based e-gun depended linearly on the e-beam current, demonstrating a maximum output optical power of 1 W at a pump current of 65 mA [121], which approximately corresponds to the data obtained in [119] for a similar MOCVD-grown structure, described above. In the e-guns with a plasma ferroelectric cathode, the temporal shape of the e-beam pulse has a complex character, as shown in Figure 31b, where the lower curve shows a sequence of several short e-beam current pulses with a maximum current up to 1.8 A and a total duration of 0.5 μs. The upper curve in this figure shows the corresponding change in the output optical power. By integrating the output-power pulse, the average energy of each pulse can be calculated. Figure 31c shows the linear dependence of this parameter on the discharge voltage (e-energy) in an e-gun with a plasma cathode, the maximum value of which is 5 μJ per pulse at a voltage (e-energy) of 12.5 kV (keV).

Preprints (www.preprints.org) | NOT PEER-REVIEWED | Posted: 20 June 2023 doi:10.20944/preprints202306.1422.v1

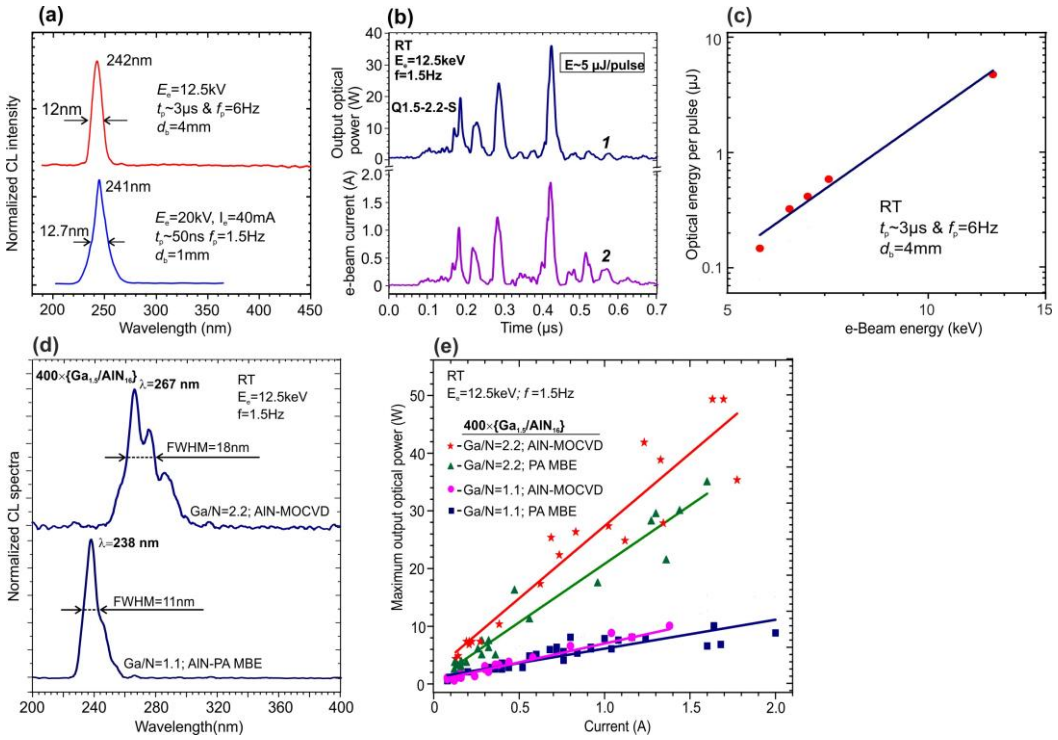

Figure 31. (a) Normalized CL-RT spectra of the {$GaN_{1.5}/AlN_{22}$} MQW structures, measured using various e-guns with a LaB_6 cathode (lower blue spectrum) and plasma ferroelectric cathode (upper red one) [120]. (b) The output optical power waveform (upper, blue) from the 360×{$GaN_{1.5}/AlN_{22}$} MQW structure excited by an e-beam current at E_e = 12.5 keV, with the waveform shown in the lower purple curve [121]. (c) Dependence of the output UVC-optical emitted by 400×{$GaN_{1.5}/AlN_{22}$} MQW structure per excitation pulse on the voltage applied to a plasma ferroelectric cathode of the e-gun [120].(d) Normalized CL-RT spectra excited with a pulse e-gun with plasma cathode at the E_e = 12.5 keV, which were measured in 400×{$GaN_{1.5}/AlN_{16}$} MQW structures grown under various Ga/N_2* flux ratio and different AlN-templates). (e) Dependences of the output optical power on the current of an energy of 12.5 keV, measured for different 400×{$GaN_{1.5}/AlN_{16}$} MQW structures. The lines are drawn in accordance with the linear interpolation of the experimental data [121].

Studies of the optical properties of 400×{$GaN_{1.5}/AlN_{16}$} MQW structures grown at different Ga/N_2* ratios and templates obtained either by MOCVD or by a combination of MOCVD and PA BE were carried out using measurements of the PL and CL spectra excited by 4th harmonic of a Ti-sapphire laser and various types of the e-guns emitting e-beam current in the range from 30 nA up to 2A, respectively [121]. All spectra showed a maximum blue shift from 260 – 270 nm to 230 – 240, as well as the narrowing of single peaks for the MQW structures grown at a lower Ga/N_2* ratio. Comparison of these spectra with the spectra of test GaN_m/AlN_{16} MQW structures with integer values of QW thicknesses m = 1 and 2, as well as with data from studies of the structural properties of MQW structures by AFM, XRR, HAADF STEM led to the conclusion that various quantum-size objects are formed depending on the growth conditions. In the case of large values of Ga/N_2*, the formation of local islands occurs with an effective thickness of 2 ML on atomically smooth terraces with a lateral size of 20 – 30 nm up to the whole width of the terrace. In contrast, the structures grown at a reduced Ga/N_2* ratio of 1.1 exhibited the formation of higher-density quantum disks with a thickness of 1 ML and smaller lateral dimensions, which corresponds to a transition from pure spiral step-flow growth mode to a mixed-growth mode with reduced adatom mobility.

The optical properties of the ML-thick QW structures are determined by excitons up to RT, as it was predicted theoretically [104] and experimentally demonstrated in [126]. It should also be noted that there is a relatively small difference between the PL and CL spectra for the MQW structures grown on AlN templates formed either by PA MBE only or sequential MOCVD and PA MBE. This implies that the characteristic size of charge carrier localization regions is much smaller than the average distance between the defect centers, and for quantum disks the distance to a spiral in of no importance.

Finally, the analysis of the CL spectra excited by plasma cathode e-gun allowed one to plot the dependences of peak output optical power on the e-beam current, which are presented in Figure 31e.

 doi:10.20944/preprints202306.1422.v1

These power dependences are linear for all MQW structures within all ranges of output optical power variations, i.e., the droop regime was not yet attained. Figure 31e shows that the highest pulse power up to 50 W at a wavelength of 267 nm was achieved for the structure grown under highly metal-enriched conditions on MOCVD/PAMBE AlN template. The same MQW structures grown on the PA MBE AlN template emitted power at almost the same wavelength of 265 nm, and demonstrated somewhat lower power values of about 35 W. The maximum power value of 10 W at a wavelength of 238 nm was observed for structures with 1.5 ML-thick MQWs grown under a low Ga/N flux ratio of 1.1 on both types AlN/*c*-Al_2O_3 templates.

The results demonstrated above showed that e-beam pumping of ML-thick GaN/AlN MQW structures allows one to obtain high intensity UVC-emission in the spectral range 240 − 260 nm with peak optical powers up to several Watts and more. However, the wall-plug efficiency of the first e-beam pumped UV-C emitters was extremely low, only 0.1 − 0.3%, and further optimization of the MQW structure design and the e-beam pumping scheme are required to improve this parameter.

Progress in the development of e-beam pumped UVC emitters with different design and grown using various technology and growth conditions is presented in Table 2.

Preprints (www.preprints.org) | NOT PEER-REVIEWED | Posted: 20 June 2023 doi:10.20944/preprints202306.1422.v1

Table 2. - Main results for e-beam pumped UVC emitters.

№	Emitter (Powder/Layer/ MQW structure)	Technology	λ	Output optical power		e-beam				WPE (IQE)	Life time	Year, Institute	Ref.
				Pulse (Scan)	cw-	Cathode	Energy	Current	Area				
			nm	mW	mW		keV	mA	cm^2	%	hrs		
1	Pyro-BN Powder	HP HT	225		0.2	W-TE	8	0.05	0.2	0.5	>150	2009, National Institute for Materials Science	[84]
2	8×{$Al_{0.69}Ga_{0.31}N$(1nm)}/ AlN(15nm)	MO CVD	240		100	W-TE	8	0.05	0.002	40	1	2010, Kyoto Univ.	[85]
3	AlGaN:Si(800nm)/AlN Layer	MO CVD	247		2.2	TE	10	0.1	0.003	0.24	>2·10^3	2011, Mie Univ. Hamamatsu	[86]
4	10×{$Al_{0.7}Ga_{0.3}N$(3nm)/ AlN(3нм)	MO CVD	240		20	Graphe-ne -FE	7.5	0.08	7	3–4	>5·10^3	2012, Stanley Electric corp.& Nagoya Univ.	[63]
5	70×$Al_{0.6}Ga_{0.4}N$:Si(1.5nm)/ $Al_{0.75}Ga_{0.25}N$:Si(7nm)	MO CVD	256		15	TE	10	0.2	0.002	0.75	-	2013, Mie Univ.& Hamamatsu	[87]
6	40×{3×[$(GaN)_1$/ $(Al_{0.75}Ga_{0.25}N)_2$]/ $(Al_{0.75}Ga_{0.25}N)_{124}$}	PA MBE	270	60	4.7	W-TE	ps:32p cw:20	ps:1.2 cw:0.1	0.5	0.19 0.24	-	2015, IOFFE	[99]

Preprints (www.preprints.org) | NOT PEER-REVIEWED | Posted: 20 June 2023 doi:10.20944/preprints202306.1422.v1

7	40×{3×[(GaN)$_1$/(Al$_{0.75}$Ga$_{0.25}$N)$_2$]/(Al$_{0.75}$Ga$_{0.25}$N)$_{124}$}		PA MBE	285	160	39	W-TE	ps:20 cw:15	ps:1.1 cw:0.7	ps:3·10^{-4} cw:0.8	ps:0.86 cw:0.43	-	2016, Peking Univ.& IOFFE	[101]
8	10×Al$_{0.56}$Ga$_{0.44}$N(1.5nm)/Al$_{0.9}$Ga$_{0.1}$N(40nm)		MO CVD	246	230	-	W-TE	p:12	p:4.4	p:0.07	p:0.43	-	2016, Palo-Alto & TU-Berlin	[57]
9	360×{GaN$_{1.5}$/AlN$_{22}$}		PA MBE	235	150	28	W-TE	ps:20 cw:15	ps:1.0 cw:0.45		ps: 0.75 cw: 0.42		2018, IOFFE	[106]
10	5×Al$_{0.47}$Ga$_{0.53}$N/Al$_{0.56}$Ga$_{0.44}$N		MO CVD	279	-	30	CNT	3	0.8	3.03	1.25		2019, Kying Univ. Korea	[65]
11	100×{GaN$_3$/AlN$_{40}$} 100×{GaN$_2$/AlN$_{40}$} 100×{GaN$_1$/AlN$_{40}$} 150×{GaN$_2$/AlN$_{40}$}		MO CVD	265 243 232 258	179 123 25 2200	53 39 0.8	TE TE TE LaB$_6$	Ps:20 Ps:20 Ps:20 Ps:18	1.2 1.2 1.0 Ps:37	0.01 0.01 0.01 0.01	0.75 0.51 0.13 0.33		2019, Peking Univ.& IOFFE	[119]
12	Al$_{0.73}$Ga$_{0.27}$N/AlN		MO CVD	233	-	6.4	CNT	4	0.5	2.83	0.32	-	2020, Kying Univ. Korea	[67]
13	NW-88×{(Al$_x$Ga$_{1-x}$N) (x=0,0.1)/AlN (3-4нм)	(0.65-1.5нм)	PA MBE	258-340	-	-	W-TE	2-15	<120 pA	-	IQE: 22-63%	-	2020, Univ. Grenoble-Alpes	[109]
14.	NW-88×{(Al$_x$Ga$_{1-x}$N) (0≤x≤0.1)/AlN (3-4нм)	(0.65-1.5нм)	PA MBE	258-340				3-10	0.4	0.13 (4mmdia)	IQE: >60%		2020, Univ. Grenoble-Alpes	[110]
15	100×{QD-QW(Al$_x$Ga$_{1-x}$N)		PA MBE	244-335	-		W-TE	3-10	0.8	0.13 (4mm	IQE: 33-54%		2020,	[111]

Preprints (www.preprints.org) | NOT PEER-REVIEWED | Posted: 20 June 2023 doi:10.20944/preprints202306.1422.v1

	(0.65-1.5нм) (x=0,0.1)/ AlN(3-4нм)								Dia)		Univ. Grenoble-Alpes	
16.	Bulk k-Al_2O_3 wafer		226-400	-	Peak:1.5	CNT	10	1.3	9.6	Peak: 0.01	2020, Kying Univ. Korea	[66]
17.	18×{GaN(2.1nm)/ $Al_{0.36}Ga_{0.64}N$(9nm)}	MO CVD	330		225	CNT	7	1	~20	3.6	2021, Chonnam Nat. Univ.	[68]
18	400×{$GaN_{1.5}/AlN_{16}$}	PA MBE	240 242	10^3 (11.8·10^3) 5μJ/ Pulse	-	LaB_6 TE PC	P:20 P:12.5	P:65 P:450	0.008 1mm) 0.13 (4mm Dia)	0.08 0.2	2021, IOFFE& Peking Univ.	[120]
19	100×{$GaN_1/Al_xGa_{1x}N_2$/ AlN_{40}} (x = 0.6)	MO CVD	248		420 702	CNT	8 8	1 3	2″	5.25	2022 Peking Univ.	[118]
20	400×{$GaN_{1.5}/AlN_{16}$}	PA MBE	238-265	15W 50W	- -	TE, PC	10 12.5	30нА 2A	1μm 4mm	0.1-0.3	2021, IOFFE& Peking Univ.	[121]

 doi:10.20944/preprints202306.1422.v1

6. Conclusions

Electron-beam pumped light emitters operating in UVC wavelength range (220-280 nm) and especially in its far-UVC subrange (~230 nm) are an attractive alternative to UVC LEDs, as they eliminate the critical problem of acceptor and donor doping of Al-rich AlGaN layers and significantly increase the output optical power of a single device. Such devices can be used in devices for the environmentally friendly and safe optical disinfection of air/water/surface, in spectroscopic devices for highly sensitive detecting various substances, in NLOS communication systems *etc.*

At present, various types of e-guns have been developed with varying degrees of industrial mass-production, ranging from the most common e-guns with thermionic cathodes (W- or LaB_6-based) to modern e-emitters using either large-area CNT-based field emission cathodes or high-current plasma cathodes of various type. The typical AlGaN-based MQW heterostructures pumped by an e-beam demonstrate UVC-emission in the spectral range 240-280 nm.

Using thermionic e-guns with conventional tungsten cathodes operated at typical anode voltage 10-20 kV and e-beam currents of few mA, the output optical power of UVC-radiation can reach several hundred milliwatts in a pulsed excitation mode and several tens of milliwatts in a cw-mode. The efficiency of excitation of UVC radiation does not exceed 1%.

An increase in the e-beam current up to several tens of milliamps is possible for e-guns with thermionic cathodes based on hexaboride compounds of rare earth metals (LaB_6, etc.), operating in a pulsed mode. The UVC-emitters with these e-guns achieve peak output optical powers of up to 1 and 2 W with wavelengths around 240 and 258 nm, respectively. However, the excitation efficiency in such UVC emitters remains extremely low (<<1%).

Significantly higher excitation efficiency up to 5.2% is achieved in AlGaN-MQW UVC-emitters pumped by e-guns with cold field emission cathodes based on graphene nanotips or CNTs deposited or formed on large area substrates up to 2 inches in diameter. The output optical power of these UVC-emitters can reach 700 mW at 248 nm when cw-excited by a CNT e-gun with an operating voltage of less than 10 kV and a current of about 1 mA, which can be provided by compact power supplies.

The maximum peak output optical power up to several tens of watts is observed in UVC-emitters pumped by a high-current pulsed e-beam (up to 2 A) generated by an e-gun with a plasma ferroelectric cathode. However, in this case, the quantum efficiency does not exceed 1%.

The most e-beam pumped UVC-emitters used MQW structures in the (Al,Ga)N system, grown using MOCVD or PA MBE. Removing the requirement for the conductivity of light-emitting heterostructures in e-beam pumped UVC-emitters allows the use of $Al_xGa_{1-x}N$/AlN heterostructures or even those based on GaN/AlN binary alloys. In the latter case, for a short-wavelength shift of the output radiation to the desired UVC range of 230–260 nm, it is necessary to reduce the QW thickness to 1 – 2 ML, which is currently provided by both PA MBE and MOCVD technologies. Moreover, the ML-range of QW thicknesses leads to a significant weakening of the quantum-confined Stark effect and the elimination of harmful switching from the TE- to TM-polarized mode of the output radiation. Both effects play a significant role in reducing the quantum efficiency and light extraction efficiency in AlGaN-based MQW structures with a high Al-content and conventional thickness of 1–2 nm.

At present, the maximum values of the internal quantum yield and output optical power have been achieved for structures with a nominal QW thickness of about 1.5ML, a number of QWs up to 400, and a total thickness of the MQW structure up to 2 μm. In addition, the possibility of a controlled change in the emission wavelength in the range from 238 to 265 nm with maximum output optical powers of 10 and 50 W, respectively, was demonstrated for the structures grown on *c*-Al_2O_3 substrates. It is also important that such structures exhibit linear non-saturated power dependencies on the pulsed pump current up to maximum values.

It is expected that the production of e-beam pumped UVC emitters with high output optical power and high efficiency in the entire wavelength range of 220-270 nm to meet current demand will be ensured in the near future.

Author Contributions: Conceptualization, V.J., V.K. and X.W.; writing—preparation of the original draft, V.J., V.K. and X.W.; writing—review and editing, V.K.; validation, V.J.; visualization, V.J., V.K., and X.W.; supervision, V.J.; project administration, V.J., X.W.; funding acquisition, V.J., X.W. All authors have read and agreed to the published version of the manuscript.

Funding: This research was funded by Ministry of science and higher education of the Russian Federation (Agreement № 075-15-2022-1224, "BiO-LIGHT").

Data Availability Statement: Data sharing not applicable.

Conflicts of Interest: The authors declare no conflict of interest.

References

1. Kneissl, M. in III-Nitride Ultraviolet Emitters: Technology and Applications, ed. M. Kneissl and J. Rass (Springer, Cham, 2016) Springer Series in Material Science, Vol. 227, Chap. 1.
2. Amano, H.; Collazo, R.; Santi, C.D.; Einfeldt S.; Funato M.; Glaab J.; Hagedorn S.; Hirano A.; Hirayama H.; Ishii, R.; Kashima, Y.; Kawakami Y.; Kirste, R.; Kneissl, M.; Martin, R.; Mehnke, F.; Meneghini, M.; Ougazzaden, A.; Parbrook, P.J.; Rajan, S.; Reddy, P.; Römer, F.; Ruschel, J.; Sarkar, B.; Scholz F.; Schowalter, L. J.; Shields, P.; Sitar, Z.; Sulmoni, L.; Wang, T.; Wernicke, T.; Weyers, M.; Witzigmann, B.; Wu.; Y.R., Wunderer, T., Zhang, Y. The 2020 UV emitter roadmap, *J. Phys.D: Appl.Phys*. **2020**, *53*, 503001. https://doi.org/1088/1361-6463/aba64c
3. Sharma, V.K.; Demir, H.V. Bright Future of Deep-Ultraviolet Photonics: Emerging UVC Chip-Scale Light-Source Technology Platforms, Benchmarking, Challenges, and Outlook for UV Disinfection, *ACS Photonics* **2022**, *9*, 1513−1521. https://doi.org/10.1021/acsphotonics.2c00041
4. Zollner, C. J.; DenBaars, S. P.; Speck, J. S.; Nakamura, S. Germicidal ultraviolet LEDs: a review of applications and semiconductor technologies, *Semicond. Sci. Technol*. **2021**, 36, 123001 (39pp). https://doi.org/10.1088/1361-6641/ac27e7
5. Hsu, T.C.; Teng Y.T.; Yeh Y.W.; Fan, X.; Chu, K. H.; Lin S.H.; Yeh, K.K.; Lee, P.T.; Lin, Y.; Chen, Z., Wu, T.; Kuo H.V. Perspectives on UVC LED: its progress and application, *Photonics* **2021**, *8*, 196. https://doi.org/10.3390/photonics8060196
6. Chen, Y.; Ben, J.; Xu, F.; Li, J.; Chen, Y.; Sun, X.; Li, D. Review on the Progress of AlGaN-based Ultraviolet Light-Emitting Diodes, *Fundamental Research* **2021**, **1**, 717–734. https://doi.org/10.1016/j.fmre.2021.11.005
7. Mondal, R.K.; Adhikari, S.; Chatterjee, V.; Pal, S. Recent advances and challenges in AlGaN-based ultra-violet light emitting diode technologies, *Mater. Res. Bull*. **2021**, *140*, 111258. https://doi.org/10.1016/j.materresbull.2021.111258
8. Zhao, S.; Lu, J.; Hai, X.; Yin, X. AlGaN Nanowires for Ultraviolet Light-Emitting:Recent Progress, Challenges, and Prospects, *Micromachines* **2020**, *11*, 125; https://doi.org/10.3390/mi11020125
9. UVC LED Beyond Covid-19: Performance Analysis and Comparison Report 2023, https://www.yolegroup.com/product/report/uvc-led-beyond-covid-19-performance-analysis-and-comparison-report-2023/
10. Kneissl, M.; Seong, T.-Y.; Han, J.; Amano, H. The emergence and prospects of deep-ultraviolet light-emitting diode technologies, *Nature Photonics* **2019**, 13, 233–244. https://doi.org/10.1038/s41566-019-0359-9
11. Knauer, A.; Kolbe, T.; Hagedorn, S.; Hoepfner, J.; Guttmann, M.; Cho, H. K.; Rass, J.; Ruschel, J.; Einfeldt, S.; Kneissl, M.; Weyers, M. Strain induced power enhancement of far-UVC LEDs on high temperature annealed AlN templates, *Appl. Phys. Lett.* **2023**, *122*, 011102. https://doi.org/10.1063/5.0134253
12. Sarkar, B.; Washiyama, S.; Breckenridg, M. H.; Klump, A.; Baker, J. N.; Reddy, P.; Tweedie, J.; Mitab, S.; Kirste, R.; Irving, D. L.; Collazo, R.; Sitar, Z. N- and P- type Doping in Al-rich AlGaN and AlN, *ECS Transactions* **2018**, 86 (12), 25-30. https://doi.org/10.1149/08612.0025ecst
13. Wang, J.; Wang, M.; Xu, F.; Liu, B.; Lang, J.; Zhang, N.; Kang, X.; Qin, Z.; Yang, X.; Wang, X.; Ge, W.; Shen, B. Sub-nanometer ultrathin epitaxy of AlGaN and its application in efficient doping, *Light: Science & Applications*, **2022**, 11, 71. https://doi.org/10.1038/s41377-022-00753-4
14. Li, D.; Jiang, K.; Sun, X.; Guo, C. AlGaN photonics: recent advances in materials and ultraviolet devices, *Adv. Opt. Photonics*, **2018**, *10*, 43-110. https://doi.org/10.1364/AOP.10.000043
15. Li, L.; Y. Zhang, S. Xu, W. Bi, Z.H. Zhang, H.C. Kuo, On the Hole Injection for III-Nitride Based Deep Ultraviolet Light-Emitting Diodes, *Materials* **2017**, *10*, 1221. https://doi.org/10.3390/ma10101221
16. Liang, Y.-H.; Towe, E. Progress in efficient doping of high aluminum-containing group III-nitrides, *Appl. Phys. Rev*. **2018**, 5, 011107. https://doi.org/10.1063/1.5009349
17. Downes A.; Blunt, T.P. Research on the effect of light upon bacteria and other organisms. *Proc. Roy Soc London* **1877**, 26, 488–500. https://doi.org/10.1098/rspl.1877.0068
18. Barnard J.; Morgan H. The physical factors in phototherapy, *Brit. Med. J*. **1903**, 2, 1269–1271. https://doi.org/10.1136/bmj.2.2237.1269
19. von Recklinghausen, M. The Ultra-Violet rays and their application for the sterilization of water, *J. Franklin Institute*, **1914**, 1057–1062, 681–704.
20. Kowalski, W. Ultraviolet Germicidal Irradiation Handbook UVGI for Air and Surface Disinfection, © Springer-Verlag Berlin Heidelberg 2009, ISBN 978-3-642-01998-2 e-ISBN 978-3-642-01999-9 Springer Heidelberg Dordrecht London New York. https://doi.org/10.1007/978-3-642-01999-9

21. Raeiszadeh, M.; Adeli, B. A Critical Review on Ultraviolet Disinfection Systems against COVID-19 Outbreak: Applicability, Validation, and Safety Considerations, *ACS Photonics* **2020**, 7, 2941–2951. https://doi.org/10.1021/acsphotonics.0c01245
22. de Abajo, F. J. G.; Hernández, R. J., Kaminer, I.; Meyerhans, A.; Rosell-Llompart, J.; Sanchez-Elsner, T. Back to Normal: An Old Physics Route to Reduce SARS-CoV-2 Transmission in Indoor Spaces, *ACS Nano* **2020**, 14, 7704−7713. https://dx.doi.org/10.1021/acsnano.0c04596
23. Blatchley, E. R.; Brenner, D. J.; Claus, H.; Cowan, T. E.; Linden, K. G.; Liu, Y.; Mao, T.; Park, S.-J.; Piper, P. J.; Simons, R. M.; Sliney, D. H. Far UV-C radiation: An emerging tool for pandemic control, *Critical Reviews in Environmental Science and Technology* **2023**, *53*(6), 733–753. https://doi.org/10.1080/10643389.2022.2084315
24. Epelle, E. I.; Macfarlane, A.; Cusack, M.; Burns, A.; Mackay, W. G.; Rateb, M. E.; Yaseen, M. Application of Ultraviolet-C Radiation and Gaseous Ozone for Microbial Inactivation on Different Materials, *ACS Omega* **2022**, 7, 43006−43021. https://doi.org/10.1021/acsomega.2c05264
25. Singh, H.; Bhardwaj, S. K.; Khatri, M.; Kim, K.-H.; Bhardwaj, N. UVC radiation for food safety: An emerging technology for the microbial disinfection of food products, *Chem. Eng. J.* **2021**, 417, 28084. https://doi.org/10.1016/j.cej.2020.128084
26. Internationale Beleuchtungskommission, UV-C photocarcinogenesis risks from germicidal lamps, Publication CIE **2010**, 187, 1 ISSN 1011-6567 CIE
27. Forbes, P. D.; Cole, C. A.; deGruijl, F. Origins and evolution of photocarcinogenesis action spectra, including germicidal UVC, *Photochem. and Photobiol*., **2021**, *97*, 477-484. https://doi.org/10.1111/php.13371
28. Barnard, I. R.; Eadie, M.; Wood, E.K. Further evidence that far-UVC for disinfection is unlikely to cause erythema or pre-mutagenic DNA lesions in skin, *Photodermatol. Photoimmunol. Photomed*. **2020**, *36*(6), 476–477. https://doi.org/10.1111/phpp.12580
29. Buonanno, M.; Ponnaiya, B.; Welch, D.; Stanislauskas, M.; Randers-Pehrson, G.; Smilenov, L.; Lowy, F. D.; Owens, D. M.; Brenner, D. J. Germicidal efficacy and mammalian skin safety of 222-nm UV light, *Radiation Research*, **2017**, *187(4)*, 483–491. https://doi.org/10.1667/RR0010CC.1
30. Yamano, N.; Kunisada, M.; Kaidzu, S; Sugihara, K.; Nishiaki-Sawada, A.; Ohashi, H.; Yoshioka, A.; Igarashi, T.; Ohira, A.; Tanito, M.; Nishigori, C. Long-term effects of 222-nm ultraviolet radiation C sterilizing lamps on mice susceptible to ultraviolet radiation, *Photochemistry and Photobiology* **2020**, 96(4), 853–862. https://doi.org/10.1111/php.13269
31. American Conference of Governmental Industrial Hygienists (ACGIH), 2022 TLVs and BEIs: Based on the documentation of the threshold limit values for chemical and physical agents & biological exposure indices. ACGIH **2022**, ISBN 9781607261520.
32. Graeffe, F.; Luo, Y.; Guo, Y.; Ehn, M. Unwanted Indoor Air Quality Effects from Using Ultraviolet C Lamps for Disinfection, *Environ. Sci. Technol. Lett*. **2023**, *10*, 172−178. https://doi.org/10.1021/acs.estlett.2c00807
33. Yoshiyama, K. O.; Okamoto, N. L.; Hidema, J.; Higashitani, A. 222 nm far-UVC efficiently introduces nerve damage in Caenorhabditis elegans, PLoS ONE **2023**, *18(1)*, e0281162. https://doi.org/10.1371/journal.pone.0281162
34. Chitraningruma, N.; Y. N. Wijayanto, Y. N.; Arisesa, H.; Sakti, I.; Mahmudin, D.; Prawara, B.; Kurniadi, D. P.; Daud, P. The Optical Characteristics of 20 Watt Far-UVC Light and Its Application for Disinfection Chamber, Jurnal Elektronika dan Telekomunikasi (JET) **2022**, *22(2)*, 57-62. https://doi.org/10.55981/jet.502
35. Eadie, E.; Hiwar, W.; Fletcher, L.; Tidswell, E. ; O'Mahoney, P.; Buonanno, M.; Welch, D.; Adamson, C. S.; Brenner, D. J.; Noakes, C.; Wood, K. Far-UVC (222 nm) efficiently inactivates an airborne pathogen in a room-sized chamber, Sci. Rep. **2022**, *12*, 4373. https://doi.org/10.1038/s41598-022-08462-z
36. Joshi, D.; Kumar, D.; Maini, A. K.; Sharma, R. C. Detection of biological warfare agents using ultraviolet-laser induced fluorescence LIDAR, Spectrochim. Acta A Mol. Biomol. Spectrosc. **2013**; *112*, 446-56. https://doi.org/10.1016/j.saa.2013.04.082
37. DeFreez, R. LIF Bio-Aerosol Threat Triggers: Then and Now, Optically Based Biological and Chemical Detection for Defence V, ed. by J. C. Carrano, C. J. Collins, *Proc. of SPIE* **2009**, *7484*, 74840H. https://doi.org/10.1117/12.835088
38. Hug, W. F.; Bharti, R.; Sijapati, K.; Beegle, L. W.; Reid, R.D. Improved sensing using simultaneous deep-UV Raman and fluorescence detection – II, Chemical, Biological, Radiological, Nuclear, and Explosives (CBRNE) Sensing XV, edited by A. W. Fountain III, *Proc. of SPIE* **2014**, *9073*, 90730I,. https://doi.org/10.1117/12.2053069
39. Reismaa, P. S.; Erme, E.; Vaher, M.; Kulp, M.; Kaljurand, M.; Mazina-Šinkar, J. In situ Determination of Illegal Drugs in Oral Fluid by Portable Capillary Electrophoresis with Deep UV Excited Fluorescence Detection, *Anal. Chem*. **2018**, *90*, 10, 6253–6258. https://doi.org/10.1021/acs.analchem.8b00911
40. D'Elia, V.; Montalvo, G.; García Ruiz, C.; Ermolenkov, V. V.; Ahmed, Y.; Lednev, I. K. Ultraviolet resonance Raman spectroscopy for the detection of cocaine in oral fluid, *Spectrochim. Acta A* **2018**, *188*, 338–340. http://dx.doi.org/10.1016/j.saa.2017.07.010

41. Kumar, V.; Holtum, T.; Voskuhl, J.; Giese, M.; Schrader, T.; Schlücker, S. Prospects of ultraviolet resonance Raman spectroscopy in supramolecular chemistry on proteins, *Spectrochim. Acta A* **2021**, *254*, 119622. https://doi.org/10.1016/j.saa.2021.119622
42. Hollis, J.R.; Ireland, S.; Abbey, W. et al., Deep-ultraviolet Raman spectra of Mars-relevant evaporite minerals under 248.6nm excitation, *Icarus* **2020**, 351,113969. https://doi.org/10.1016/j.icarus.2020.113969
43. Fox, A. C.; Jakubek, R. S.; Eigenbrode, J. L. Changes in the Raman and fluorescence spectroscopic signatures of irradiated organic-mineral mixtures: Implications for molecular biosignature detection on Mars, *J. Geophys. Res. Planets* **2023**, *128*, e2022JE007624. https://doi.org/10.1029/2022JE007624
44. Nikishin, S.; Bernussi, A.; Karpov, S. Towards Efficient Electrically-Driven Deep UVC Lasing: Challenges and Opportunities, *Nanomaterials* **2023**, *13*, 185. https://doi.org/10.3390/nano13010185
45. Majumdar, A. K. Chapter 5 Non-Line-Of-Sight (NLOS) Ultraviolet and Indoor Free-Space Optical (FSO) Communications, in A. K. Majumdar Advanced Free Space Optics (FSO) A Systems Approach, Springer Series in Optical Sciences, **2015** Volume 186, Springer New York Heidelberg Dordrecht London. https://doi.org/10.1007/978-1-4939-0918-6
46. Belov, V. V.; Juwiler, I.; Blaunstein, N.; Tarasenkov, M. V.; Poznakharev, E. S. NLOS Communication: Theory and Experiments in the Atmosphere and Underwater, *Atmosphere* **2020**, *11*, 1122. https://doi.org/10.3390/atmos11101122
47. Guo, L.; Guo, Y.; Wang, J.; Wei, T. Ultraviolet communication technique and its application, *J. Semicond* **2021**, *42*, 081801. https://doi.org/10.1088/1674-4926/42/8/081801
48. Yoo, S. T.; Lee, J. Y.; Rodiansyah, A.; Yune, T. Y.; Park, K. C. Far UVC light for E. coli disinfection generated by carbon nanotube cold cathode and sapphire anode, *Curr. Appl. Phys.* **2021**, *28* 93–97. https://doi.org/10.1016/j.cap.2021.05.007
49. DeFreez, R.; Hug, W.; Reid, R.; Bhartia, R. New deep-ultraviolet sources for detecting biological threats, *SPIE Newsroom* **2010**. https://doi.org/10.1117/2.1201001.002570
50. Kang, Y.; Zhao, J.; Wu, J.; Zhang, L.; Zhao, J. Superior Deep-Ultraviolet Source Pumped by an Electron Beam for NLOS Communication, *IEEE Trans. Electron Devices* **2020**, *67(8)*, 3391 – 3394. https://doi.org/10.1109/TED.2020.3004122
51. Cuesta, S.; Harikumar, A.; Monroy, E. Electron beam pumped light emitting devices, *J. Phys. D: Appl. Phys*. **2022**, *55*, 273003. https://doi.org/10.1088/1361-6463/ac6237
52. Harikumar, A. Développement de nanostructures à base d'AlGaN pour la fabrication de com- posants émetteurs de lumière UV à pompage électronique. Physique [physics]. Université Grenoble Alpes [2020-..], 2022. Français. NNT : **2022** GRALY039. tel-03813791
53. Yu, Y.; Han, D.; Wei, H.; Tang, Z.; Luo, L.; Hong, T.; Shen, Y.; Zheng, H.; Wang, Y.; Wang, R.; Zhu, H.; Deng, S. Aluminum Nitride Ultraviolet Light-Emitting Device Excited via Carbon Nanotube Field-Emission Electron Beam, *Nanomaterials* **2023**, *13*, 1067. https://doi.org/10.3390/nano13061067
54. Jmerik, V.; Toropov, A.; Davydov, V.; Ivanov, S. Monolayer-Thick GaN/AlN Multilayer Heterostructures for Deep-Ultraviolet Optoelectronics, *Phys. Status Solidi RRL* **2021**, *15*(9), 2100242. https://doi.org/10.1002/pssr.202100242
55. Sheshin, E. P.; Kolodyazhnyj, A. Yu.; Chadaev, N. N.; Getman, A. O.; Danilkin, M. I.; Ozol, D. I. Prototype of cathodoluminescent lamp for general lighting using carbon fiber field emission cathode, J. *Vac. Sci. Technol. B* **2019**, *37*, 031213. https://doi.org/10.1116/1.5070108
56. Yoo, S. T.; Park, K. C.; Sapphire Wafer for 226 nm Far UVC Generation with Carbon Nanotube-Based Cold Cathode Electron Beam (C-Beam) Irradiation, *ACS Omega* **2020**, *5(25)*, 15601–15605. https://dx.doi.org/10.1021/acsomega.0c01824
57. Tabataba-Vakili, F.; Wunderer, T.; Kneissl, M.; Yang, Z.; Teepe, M.; Batres, M.; Feneberg, M.; Vancil, B.; Johnson, N.M. Dominance of radiative recombination from electron-beam-pumped deep-UV AlGaN multi-quantum-well heterostructures. Appl. Phys. Lett. **2016**, *109*, 181105. https://dx.doi.org/10.1063/1.4967220.
58. Chapter 5 Electron sources in David B. Williams C. Barry Carter, Transmission Electron Microscopy A Textbook for Materials Science, 2nd edition, Springer ScienceþBusiness Media, LLC **1996**, **2009**. New York, NY 10013, USA. 73-89.
59. Liu, H.; Zhang, X.; Ning, S.; Xiao, Y.; Zhang, J. The electronic structure and work functions of single crystal LaB_6 typical crystal surfaces, *Vacuum* **2017**, *143*, 245–250. http://dx.doi.org/10.1016/j.vacuum.2017.06.029
60. Çetinkaya, H.; Özbey, A.; Yüncü, A. Thermionic Electron Gun Design and Prototyping, *Eur. j., eng. sci., tech*. **2021**, *23*, 702-709,. http://dx.doi.org/10.31590/ejosat.809155
61. Schmidt, P. H., Longinotti, L. D.; Joy, D. C.; Ferris, S. D.; Leamy, H. J.; Fisk, Z. Design and optimization of directly heated LaB_6 cathode assemblies for electron beam instruments, *J. Vac. Sci. Technol*. **1978**, *15*, 1554. http://dx.doi.org/10.1116/1.569786
62. Gesley, M.; Hohn, F. Emission distribution, brightness, and mechanical stability of the LaB6 triode electron gun, *J. Appl. Phys*. **1988**, *64*, 3380. http://dx.doi.org/10.1063/1.341522

63. Matsumoto, T.; Iwayama, S.; Saito, T.; Kawakami, Y.; Kubo, F.; Amano, H. Handheld deep ultraviolet emission device based on AlN QWs and graphene nanoneedle field emitters, *Opt. Express* **2012**, 20, 24320–24329. http://dx.doi.org/10.1364/OE.20.024320
64. Yoo, S. T.; Hong, J. H.; Kang, J. S.; Park, K. C. Deep-ultraviolet light source with a carbon nanotube cold-cathode electron beam, *J. Vac. Sci. Technol B* **2018**, *36*, 02C103. https://doi.org/10.1116/1.5004621
65. Yoo, S. T.; So, B.; Lee, H. I.; Nam, O.; Park, K. C. Large area deep ultraviolet light of $Al_{0.47}Ga_{0.53}N/Al_{0.56}Ga_{0.44}N$ multi quantum well with carbon nanotube electron beam pumping, *AIP Advances* **2019**, *9*, 075104. https://doi.org/10.1063/1.5109956
66. Tawfik, W. Z.; Kumar, C.M. M.; Park, J.; Shim, S. K.; Lee, H.; Lee, J.; Han, J. H.; Ryu, S.; Lee N.; Lee, J. K. Cathodoluminescence of 2-inch Ultraviolet-Light-Source Tube Based on the Integration of AlGaN Materials and Carbon Nanotubes Field Emitters, *J. Mater. Chem. C Mater*. **2019**, *7*, 11540–11548. https://doi.org/10.1039/C9TC03365C
67. Lee, J.; Yoo, S. T.; So, B.; Park, K. C.; Nam, O. Large-area far ultraviolet-C emission of $Al_{0.73}Ga_{0.23}N/AlN$ multiple quantum wells using carbon nanotube based cold cathode electron-beam pumping, *Thin Solid Films* **2020**, *711*, 138292. https://doi.org/10.1016/j.tsf.2020.138292
68. Mohan, M. K. C.; Shim, S. K.; Cho, M. U.; Kim, T. K.; Kwak, J. S.; Park, J.; Jang, N.; Ryu, S.-W.; Lee, N.; Lee, J. K. Ultraviolet-cathodoluminescent 330 nm light source from a 2-inch wide CNT electron-beam emission under DC electric field, *Curr. Appl. Phys*. **2021**, *28*, 72-77. https://doi.org/10.1016/j.cap.2021.04.014
69. Burdovitsin, V.; Oks, E. Hollow-cathode plasma electron gun for beam generation at forepump gas pressure, *Rev. Sci. Instrum*. **1999**, *70*, 2975. http://dx.doi.org/10.1063/1.1149856
70. Oks, E. M.; Schanin, P. M. Development of plasma cathode electron guns, *Phys. Plasmas* **1999**, *6*, 1649. http://dx.doi.org/10.1063/1.873420
71. Verma, D.K.; Pal, U.N.; Kumar, N.; Prajapati, J.; Kumar, M.; Prakash, R.; Srivastava, V. Investigation of electron beam parameters inside the drift region of plasma cathode electron gun, *J. Phys.: Conf. Ser*. **2012**, *365*, 012048. http://dx.doi.org/10.1088/1742-6596/365/1/012048
72. Burdovitsin, V. A.; Oks E. M. Discharge systems and plasma-assisted electron emission in forevacuum pressure range, Russ. Phys. J. **2021**, *63(10)*, 1678. http://dx.doi.org/10.1007/s11182-021-02221-9
73. Rosenblum, B.; Bräunlich, P.; Carrico, J. P. Thermally stimulated field emission from pyroelectric $LiNbO_3$, *Appl. Phys. Lett*. **1974**, *25*, 17. http://dx.doi.org/10.1063/1.1655260
74. Rozenman, G. I.; Okhapkin, V. A.; Chepelev, Yu. L.; Shur, V. Ya. Electron emission during the switching of ferroelectric lead germanate, *Pis'ma Zh. Eksp. Teor. Fiz. (JETP Letters)* **1984**, *39(9)*, 397-399.
75. Ivers, J. D.; Schächter, L.; Nation, J. A.; Kerslick, G. S.; Advani, R. Electron beam diodes using ferroelectric cathodes, *J. Appl. Phys*. **1993**, *73*, 2667. http://dx.doi.org/10.1063/1.353062
76. Moorti, A.; Sailaj, S.; Naik, P. A.; Gupta, P. D.; Korobkin, Yu. V.; Romanov, I. V.; Rupasov, A. A.; Shikhanov, A. S. Laser-driven high-current-density pulsed electron emission from lead zirconium titanate ferroelectric ceramic, *Appl. Phys. Lett*. **2001**, *79*, 1163. http://dx.doi.org/10.1063/1.1396309
77. Einat, M.; Jerby, E.; Rosenman, G. A ferroelectric electron gun in a free-electron maser experiment, *Nucl. Instrum. Methods Phys. Res. A* **2002**, *483*, 326–330. https://doi.org/10.1016/S0168-9002(02)00337-6
78. Seo, M.; Hong, K. Characteristics of Electron Emission from a (Pb,La)(Zr,Ti)O3 Ferroelectric Cathode, *Jap. J. Appl. Phys*. **2010**, *49*, 076001. https://doi.org/10.1143/JJAP.49.076001
79. Chen, S.; Zheng, S.; Zhu, Z.; Dong, X.; Tang, C. Electron emission and plasma generation in a modulator electron gun using ferroelectric cathode, *Nucl. Instrum. Methods Phys. Res. A* **2006**, *566*, 662–667. https://doi.org/10.1016/j.nima.2006.07.049
80. Schachter, L.; Ivers, J. D.; Nation, J. A.; Kerslick G. S. Analysis of a diode with a ferroelectric cathode, *J. Appl. Phys*. **1993**, *73*, 8097. http://dx.doi.org/10.1063/1.353926
81. Riege, H. Electron emission from ferroelectrics - a review, *Nucl. Instrum. Methods Phys. Res. A* **1994**, *340(1)*, 80-89. https://doi.org/10.1016/0168-9002(94)91282-3
82. Rosenman, G.; Shur, D.; Krasik, Ya. E.; Dunaevsky, A. Electron emission from ferroelectrics, *J. Appl. Phys*. **2000**, *88*, 6109. http://dx.doi.org/10.1063/1.1319378
83. Mesyats, G. A. Electron emission from ferroelectric plasma cathodes, *Phys. - Uspekhi* **2008**, *178(1)*, 85 - 108. https://doi.org/10.3367/UFNr.0178.200801e.0085
84. Watanabe, K.; Taniguchi, T.; Niiyama, T.; Miya, K.; Taniguchi, M. Far-ultraviolet plane-emission handheld device based on hexagonal boron nitride, *Nat. Photon.* **2009**, *3*, 591-594. https://doi.org/10.1038/NPHOTON.2009.167
85. Oto, T.; Banal, R. G.; Kataoka, K.; Funato, M.; Kawakami, Y. 100 mW deep-ultraviolet emission from aluminium-nitride-based quantum wells pumped by an electron beam, *Nat. Photon*. **2010**, *4*, 767-771. https://doi.org/10.1038/NPHOTON.2010.220
86. Shimahara, Y., Miyake, H.; Hiramatsu, K.; Fukuyo, F.; Okada, T.; Takaoka, H.; Yoshida, H. Fabrication of Deep-Ultraviolet-Light-Source Tube Using Si-Doped AlGaN, *Appl. Phys. Express* **2011**, *4*, 042103. https://doi.org/10.1143/APEX.4.042103

87. Fukuyo, F.; Ochiai, S.; Miyake, H.; Hiramatsu, K.; Yoshida, H.; Kobayashi, Y. Growth and Characterization of AlGaN Multiple Quantum Wells for Electron-Beam Target for Deep-Ultraviolet Light Sources, *Jap. J. Appl. Phys*. **2013**, *52* 01AF03. http://dx.doi.org/10.7567/JJAP.52.01AF03
88. Duboz, J. Y.; Binet, F.; Dolfi, D.; Laurent, N.; Scholz, F.; Off, J.; Sohmer, A.; Briot, O.; Gil, B. Diffusion length of photoexcited carriers in GaN, *Mater. Sci. Eng. B* **1997**, *50*, 289. https://doi.org/10.1016/S0921-5107(97)00192-X
89. Yakimov, E. B. Electron-beam-induced-current study of defects in GaN; experiments and simulation, *J. Phys. Condens. Matter*. **2002**, *14*, 13069. https://doi.org/10.1088/0953-8984/14/48/352
90. Lin, Y.; Flitsyian, E.; Chernyak, L.; Malinauskas, T.; Aleksiejunas, R.; Jarašiunas, K.; Lim, W.; Pearton, S. J.; Gartsman, K. Optical and electron beam studies of carrier transport in quasibulk GaN, *Appl. Phys. Lett*. **2009**, *95*, 092101. https://doi.org/10.1063/1.3220062
91. Hocker, M.; Maier, P.; Jerg, L.; Tischer, I.; Neusser, G.; Kranz, C.; Pristovsek, M.; Humphreys, C. J.; Leute, R. A. R., Heinz, D.; Rettig, O.; Scholz, F.; Thonke, K. Determination of axial and lateral exciton diffusion length in GaN by electron energy dependent cathodoluminescence, *J. Appl. Phys*. **2016**, *120*, 085703. https://doi.org/10.1063/1.4961417
92. Brandt, O.; Kaganer, V. M.; Lähnemann, J.; Flissikowski, T.; Pfüller, C.; Sabelfeld, K. K., Kireeva, A. E., Chèze, C.; Calarco, R.; Grahn, H. T.; Jahn, U. Carrier Diffusion in GaN: A Cathodo-luminescence Study. II. Ambipolar versus Exciton Diffusion, *Phys. Rev. Applied* **2022**, *17*, 024018. https://doi.org/10.1103/PhysRevApplied.17.024018
93. Zheng, H.; Sharma, V. K.; Tsai, P.; Zhang, Y.; Lu, S.; Zhang, X.; Tan, S. T.; Demir, H. V. Engineered ultraviolet InGaN/AlGaN multiple-quantum-well structures for maximizing cathodoluminescence efficiency, *AIP Advances* **2022**, *12*, 015005. https://doi.org/10.1063/6.0001262
94. Barjon, J.; Brault, J.; Daudin, B.; Jalabert, D.; Sieber, B. Cathodoluminescence study of carrier diffusion in AlGaN, *J. Appl. Phys*. **2003**, *94*, 2755. http://dx.doi.org/10.1063/1.1593797
95. Koppe, T.; Hofsäss, H.; Vetter, U. Overview of band-edge and defect related luminescence in aluminum nitride, *J. Lumin*. **2016**, *178*, 267–281. https://doi.org/10.1016/j.jlumin.2016.05.055
96. Liu, J.; Tam, W.S.; Wong, H.; Filip, V. Temperature-dependent light-emitting characteristics InGaN/GaN diodes, *Microelectron. Reliab.* **2009**, *49*, 38–41, https://doi.org/10.1016/j.microrel.2008.10.002
97. Yasan, A.; McClintock, R.; Mayes, K.; Kim, D.H.; Kung, P., Razeghi, M. Photoluminescence study of AlGaN-based 280nm ultraviolet light-emitting diodes, *Appl. Phys. Lett*. **2003**, *83*, 4083. https://doi.org/10.1063/1.1626808
98. Pinos, A.; Liuolia, V.; Marcinkevičius, S.; Yang, J., Gaska, R.; Shur, M.S. Localization potentials in AlGaN epitaxial films studied by scanning ear-field optical spectroscopy, *J. Appl. Phys*. **2011**, *109*, 113516. https://doi.org/10.1063/1.3594239
99. Ivanov, S. V.; Jmerik, V. N.; Nechaev, D. V.; Kozlovsky, V. I.; Tiberi, M. D. E-beam pumped mid-UV sources based on MBE-grown AlGaN MQW, *Phys. Status Solidi A* **2015**, *212*, 1011. https://doi.org/10.1002/pssa.201431756
100. Jmerik, V.N.; Shubina, T.V.; Mizerov, A.M.; Belyaev, K.G.; Sakharov, A.V.; Zamoryanskaya, M.V.; Sitnikova, A.A.; Davydov, V.Yu.; Kop'ev, P.S.; Lutsenko, E.V.; Rzheutskii, N.V.; Danilchik, A.V.; Yablonskii, G.P.; Ivanov, S.V. AlGaN quantum well structures for deep-UV LEDs grown by plasma-assisted MBE using sub-monolayer digital-alloying technique, *J. Crystal Growth* **2009**, *311*, 2080–2083. https://doi.org/10.1016/j.jcrysgro.2008.11.080
101. Rong, X.; Wang, X. Q.; Ivanov, S. V.; Jiang, X. H.; Chen, G.; Wang, P.; Wang, W. Y.; He, C. G.; Wang, T.; Schulz, T.; Albrecht, M.; Jmerik, V. N.; Toropov, A. A.; Ratnikov, V. V.; Kozlovsky, V. I.; Martovitsky, V. P.; Jin, P.; Xu, F. J.; Yang, X. L.; Qin, Z. X.; Ge, W. K.; Shi, J. J.; Shen, B. High-output-power ultraviolet light source from quasi-2D GaN quantum structure, *Adv. Mater*. **2016**, 28, 7978–7983. https://doi.org/10.1002/adma.201600990
102. Kamiya, K.; Ebihara, Y.; Shiraishi, K.; Kasu, M. Structural design of AlN/GaN superlattices for deep-ultraviolet light-emitting diodes with high emission efficiency, *Appl. Phys. Lett*. **2011,** *99*, 151108. https://doi.org/10.1063/1.3651335
103. Taniyasu Y.; Kasu, M. Polarization property of deep-ultraviolet light emission from *c*-plane AlN/GaN short-period superlattices, *Appl. Phys. Lett*. **2011,** *99*, 251112. https://doi.org/10.1063/1.3671668
104. Bayerl, D.; Islam, S.M.; Jones, C.M.; Protasenko, V.; Jena, D.; Kioupakis, E. Deep ultraviolet emission from ultra-thin GaN/AlN heterostructures, *Appl. Phys. Lett*. **2016**, *109*, 241102. https://doi.org/10.1063/1.4971968
105. Liu, C.; Ooi, Y. K.; Islam, S. M.; Xing, H. (Grace), Jena, D., Zhang, J. 234 nm and 246 nm AlN-Delta-GaN quantum well deep ultraviolet light-emitting diodes, *Appl. Phys. Lett.* **2018**, *112*, 011101. https://doi.org/10.1063/1.5007835
106. Jmerik, V.N.; Nechaev, D.V.; Toropov, A.A.; Evropeitsev, E.A.; Kozlovsky, V.I.; Martovitsky, V.P., Rouvimov, S.; Ivanov, S.V. High-efficiency electron-beam-pumped sub-240-nm ultraviolet emitters based on ultra-thin GaN/AlN multiple quantum wells grown by plasma-assisted molecular-beam epitaxy on c-Al_2O_3, *Appl. Phys. Express* **2018,** *11*, 091003. https://doi.org/10.7567/APEX.11.091003

107. Jmerik, V.N.; Nechaev, D.V.; Ivanov, S.V. Kinetics of metal-rich PA molecular beam epitaxy of AlGaN heterostructures for mid-UV photonics, in *Molecular Beam Epitaxy: from Research to Mass Production*, 2nd ed.; Henini, M., Ed.; Elsevier Inc.: Amsterdam, Netherlands, Oxford, UK, Cambridge, USA, 2018; 135–179. https://doi.org/10.1016/B978-0-12-812136-8.00008-6.
108. Dimkou, I.; Harikumar, A.; Ajay, A.; Donatini, F.; Bellet-Amalric, E.; Grenier, A.; den Hertog, M I.; Purcell, S. T.; Monroy, E. Design of AlGaN/AlN Dot-in-a-Wire Heterostructures for Electron-Pumped UV Emitters, *Physica Status Solidi A* **2020**, *217(7)*, 1900714. https://doi.org/10.1002/pssa.201900714
109. Dimkou, A.; Harikumar, F.; Donatini, J.; Lähnemann, M. I.; den Hertog, Bougerol, C.; Bellet-Amalric, E.; Mollard, N.; Ajay, A.; Ledoux, G.; Purcell, S. T.; Monroy, E. Assessment of AlGaN/AlN superlattices on GaN nanowires as active region of electron-pumped ultraviolet sources, *Nanotechnology* 2020, 31, 204001. https://doi.org/10.1088/1361-6528/ab704d
110. Harikumar, F. Donatini, C. Bougerol, E. Bellet-Amalric, Q-M. Thai, C. Dujardin, I. Dimkou, S.T. Purcell, E. Monroy, Internal quantum efficiency of AlGaN/AlN quantum dot superlattices for electron-pumped ultraviolet sources, *Nanotechnology* **2020**, *31(50)*, 505205. https://doi.org/10.1088/1361-6528/aba86c
111. Widmann, F.; Daudin, B.; Feuillet, G.; Samson, Y.; Rouvie`re, J. L.; Pelekanos, N. Growth kinetics and optical properties of self-organized GaN quantum dots, *J. Appl. Phys*. **1998**, *83*, 7618. https://doi.org/10.1063/1.367878
112. Mula, G.; Adelmann, C.; Moehl, S.; Oullier, J.; Daudin, B. Surfactant effect of gallium during molecular-beam epitaxy of GaN on AlN(0001), *Phys. Rev. B* **2001**, *64*, 195406. https://doi.org/10.1103/PhysRevB.64.195406
113. Adelmann, C.; Daudin, B.; Oliver, R. A.; D. Briggs, G. A.; Rudd, R. E. Nucleation and growth of GaN/AlN quantum dots, *Phys. Rev. B* **2004**, *70*, 125427. https://doi.org/10.1103/PhysRevB.70.125427
114. Gogneau, N.; Jalabert, D.; Monroy, E.; Sarigiannidou, E.; Rouvie`re, J. L.; Shibata, T.; Tanaka, M.; Gerard, J. M.; Daudin, B. Influence of AlN overgrowth on structural properties of GaN quantum wells and quantum dots grown by plasma-assisted molecular beam epitaxy, *J. Appl. Phys*. **2004**, *96*, 1104-1110. https://doi.org/10.1063/1.1759785
115. Vermeersch, R.; Jacopin, G.; Castioni, F.; Rouvière, J.-L.; García-Cristóbal, A.; Cros, A.; Pernot, J.; Daudin, B. Ultrathin GaN quantum wells in AlN nanowires for UV-C emission, *Nanotechnology* **2023**, *34*, 275603. https://doi.org/10.1088/1361-6528/accaeb
116. Mokutani, N.; Deura, M.; Mouri, S.; Shojiki, K.; Xiao, S.; Miyake, H.; Araki, T. Control of Metal-Rich Growth for GaN/AlN Superlattice Fabrication on Face-to-Face-Annealed Sputter-Deposited AlN Templates, *Phys. Status Solidi B* **2023**, 2300061. https://doi.org/10.1002/pssb.202300061
117. T. Yamaguchi, Y. Nanishi1, Indium Droplet Elimination by Radical Beam Irradiation for Reproducible and High-Quality Growth of InN by RF Molecular Beam Epitaxy, Applied Physics Express 2 (2009) 051001. https://doi.org/10.1143/APEX.2.051001
118. Y. Wang, Y. Yuan, R. Tao, S. Liu, T. Wang, S. Sheng, P. Quach, M. Kumar CM, Z. Chen, F. Liu, X. Rong, P. Jin, M. Feng, H. Li, S. Guo, W. Ge, J. K. Lee, B. Shen, X. Wang, High-Efficiency E-Beam Pumped Deep-Ultraviolet Surface Emitter Based on AlGaN Ultra-Thin Staggered Quantum Wells, Adv. Optical Mater. 2022, 2200011. https://doi.org/10.1002/adom.202200011
119. Wang, Y.; Rong, X.; Ivanov, S.; Jmerik, V.; Chen, Z.; Wang, H.; Wang, T.; Wang, P.; Jin, P.; Chen, Y.; Kozlovsky, V.; Sviridov, D.; Zverev, M.; Zhdanova, E.; Gamov, N.; Studenov, V.; Miyake, H.; Li, H.; Guo, S.; Yang, X.; Xu, F.; Yu, T.; Qin, Z.; Ge, W.; Shen, B.; Wang, X. Deep Ultraviolet Light Source from Ultrathin GaN/AlN MQW Structures with Output Power Over 2 Watt, *Adv. Optical Mater.* **2019**, 1801763, https://doi.org/10.1002/adom.201801763
120. Jmerik, V.N.; Nechaev, D.V.; Orekhova, K.N.; Prasolov, N.D.; Kozlovsky, V.I.; Sviridov, D.E.; Zverev, M.M.; Gamov, N.A.; Grieger, L.; Wang, Y.; Wang, T.; Wang, X.; Ivanov, S. Monolayer-Scale GaN/AlN Multiple Quantum Wells for High Power e-Beam Pumped UV-Emitters in the 240–270 nm Spectral Range. *Nanomaterials* **2021**, 11, 2553. https://doi.org/10.3390/nano11102553
121. Nechaev, D.V.; Koshelev, O.A.; Ratnikov, V.V.; Brunkov, P.N.; Myasoedov, A.V.; Sitnikova, A. A.; Ivanov, S.V.; Jmerik, V.N. Effect of stoichiometric conditions and growth mode on threading dislocations filtering in AlN/c-Al_2O_3 templates grown by PA MBE, *Superlattices and Microst*. **2020**, 138, 106368. https://doi.org/10.1016/j.spmi.2019.106368
122. Koshelev, O.A.; Nechaev, D.V.; Brunkov, P.N.; Ivanov, S.V.; Jmerik, V.N. Stress control in thick AlN/c-Al2O3 templates grown by plasma-assisted molecular beam epitaxy, *Semicond. Sci. Technol*. **2021**, *36*, 035007 (13pp). https://doi.org/10.1088/1361-6641/abd63d
123. Kaneko, M.; Ueta, S.; Horita, M.; Kimoto, T.; Suda, J. Deep-ultraviolet light emission from 4H-AlN/4H-GaN short-period superlattice grown on 4H-SiC(11-20), *Appl. Phys. Lett*. **2018**, *112*, 012106. https://doi.org/10.1063/1.5006435
124. Kobayashi, H.; Ichikawa, S.; Funato, M.; Kawakami, Y. Self-Limiting Growth of Ultrathin GaN/AlN Quantum Wells for Highly Efficient Deep Ultraviolet Emitters, *Adv. Optical Mater*. **2019**, 1900860. https://doi.org/10.1002/adom.201900860

125. Jmerik, V.; Nechaev, D.; Semenov, A.; Evropeitsev, E.; Shubina, T.; Toropov, A.; Yagovkina, M.; Alexeev, P.; Borodin, B.; Orekhova, K.; Kozlovsky, V.; Zverev, M.; Gamov, N.; Wang, T.; Wang, X.; Pristovsek, M.; Amano, H.; Ivanov, S. 2D-GaN/AlN Multiple Quantum Disks/Quantum Well Heterostructures for High-Power Electron-Beam Pumped UVC Emitters, *Nanomaterials* **2023**, *13*, 1077. https://doi.org/10.3390/nano13061077
126. Toropov, A.A.; Evropeitsev, E.A.; Nestoklon, M.O.; Smirnov, D.S.; Shubina, T.V.; Kaibyshev, V.Kh.; Budkin, G.V.; Jmerik, V.N.; Nechaev, D.V.; Rouvimov, S.; et al. Strongly confined excitons in GaN/AlN Nanostructures with atomically thin GaN Layers for efficient light emission in deep-ultraviolet. *Nano Lett.* **2020**, *20*, 158–165. https://doi.org/10.1021/acs.nanolett.9b03517.